OPTOELECTRONICS

Battery-free, stretchable optoelectronic systems for wireless optical characterization of the skin

Jeonghyun Kim,[1,2]* Giovanni A. Salvatore,[1,3]*† Hitoshi Araki,[1] Antonio M. Chiarelli,[4] Zhaoqian Xie,[5,6] Anthony Banks,[1] Xing Sheng,[7] Yuhao Liu,[1] Jung Woo Lee,[1,2] Kyung-In Jang,[1] Seung Yun Heo,[1] Kyoungyeon Cho,[8] Hongying Luo,[5,9] Benjamin Zimmerman,[4] Joonhee Kim,[1] Lingqing Yan,[1] Xue Feng,[6] Sheng Xu,[10] Monica Fabiani,[4] Gabriele Gratton,[4] Yonggang Huang,[5] Ungyu Paik,[2]† John A. Rogers[1]†

Recent advances in materials, mechanics, and electronic device design are rapidly establishing the foundations for health monitoring technologies that have "skin-like" properties, with options in chronic (weeks) integration with the epidermis. The resulting capabilities in physiological sensing greatly exceed those possible with conventional hard electronic systems, such as those found in wrist-mounted wearables, because of the intimate skin interface. However, most examples of such emerging classes of devices require batteries and/or hard-wired connections to enable operation. The work reported here introduces active optoelectronic systems that function without batteries and in an entirely wireless mode, with examples in thin, stretchable platforms designed for multiwavelength optical characterization of the skin. Magnetic inductive coupling and near-field communication (NFC) schemes deliver power to multicolored light-emitting diodes and extract digital data from integrated photodetectors in ways that are compatible with standard NFC-enabled platforms, such as smartphones and tablet computers. Examples in the monitoring of heart rate and temporal dynamics of arterial blood flow, in quantifying tissue oxygenation and ultraviolet dosimetry, and in performing four-color spectroscopic evaluation of the skin demonstrate the versatility of these concepts. The results have potential relevance in both hospital care and at-home diagnostics.

INTRODUCTION

Accurate monitoring of temperature, blood pressure, oxygenation, blood flow, and electrophysiology is important in biomedical research, clinical care, and remote diagnostics of health status (1–5). Commercially available wearable devices exist predominantly in the form of mechanically hard components mounted on straps and worn on the wrist, with form factors that are ultimately limited by the size and weight of the batteries used for power supply. Wearable devices with "skin-like" properties represent a different form of technology that is now beginning to emerge from research laboratories into precommercial prototypes. Here, the devices exploit materials and layouts that lead to system-level physical properties (thicknesses, moduli, physical and thermal mass, etc.) that approximate those of the skin itself. The result is an imperceptible mode of integration with the skin through direct lamination, thereby circumventing limitations of conventional hardware to provide continuous streams of clinical quality data on physiological health (6–9). The most highly functional systems of this type require wired connection for power delivery and/or data acquisition. Soft, skin-mounted systems that operate in a fully wireless mode without the need for batteries represent the ultimate embodiment (10), although only simple examples of sensing of temperature (11), electrophysiology (12), and chemical sensing (13) have been demonstrated. The present work introduces several battery-free, wireless optoelectronic devices that exploit near-field communication (NFC) technology for multicolor light emission and detection in a manner that allows precise measurements of the optical properties of the skin, to diagnose peripheral vascular disease and evaluate coloration, and/or of color-responsive materials for environmental detection. Specific examples include devices that can monitor heart rate, tissue oxygenation, pressure pulse dynamics, ultraviolet (UV) exposure, and skin color through an integrated collection of time-multiplexed miniaturized light-emitting diodes (LEDs) and photodetectors whose signals are amplified and digitized before wireless transmission. Carefully optimized materials and mechanics designs yield form factors capable of soft and conformal lamination onto the skin, with the ability to function properly under large strain (up to 30% uniaxial) deformation. These findings suggest a foundation for technologies with wide-ranging utility in healthcare- and non–healthcare-related applications alike. These systems represent important advances over devices that require wired data transfer and conventional power sources for measurement of arterial blood oxygenation through commercial or organic LEDs and photodetectors assembled on flexible, as opposed to stretchable, supports (14–17).

[1]Department of Materials Science and Engineering, Frederick Seitz Materials Research Laboratory, University of Illinois at Urbana-Champaign, Urbana, IL 61801, USA. [2]Department of Energy Engineering, Hanyang University, Seoul 133-791, Republic of Korea. [3]Electronics Laboratory, Swiss Federal Institute of Technology, Zurich 8092, Switzerland. [4]Beckman Institute, University of Illinois at Urbana-Champaign, Urbana, IL 61801, USA. [5]Departments of Civil and Environmental Engineering, Mechanical Engineering, and Materials Science and Engineering, Center for Engineering and Health, and Skin Disease Research Center, Northwestern University, Evanston, IL 60208, USA. [6]Applied Mechanics Laboratory, Department of Engineering Mechanics, Center for Mechanics and Materials, Tsinghua University, Beijing 100084, China. [7]Department of Electronic Engineering, Tsinghua University, Beijing 100084, China. [8]Department of Electrical and Computer Engineering, Frederick Seitz Materials Research Laboratory, University of Illinois at Urbana-Champaign, Urbana, IL 61801, USA. [9]School of Aerospace Engineering and Applied Mechanics, Tongji University, Shanghai 200092, China. [10]Department of Nanoengineering, University of California San Diego, La Jolla, CA 92093, USA.
*These authors contributed equally to this work.
†Corresponding author. Email: giovanni.salvatore@ife.ee.ethz.ch (G.A.S.); upaik@hanyang.ac.kr (U.P.); jrogers@illinois.edu (J.A.R.)

RESULTS

Heart rate and temporal dynamics of arterial blood flow

The key features of a thin, stretchable wireless optoelectronic system that exploits NFC technology to monitor heart rate through measurement of backscattered light from an infrared (IR; 950 nm, AlGaAs) LED with a silicon (PIN) photodetector are highlighted in Fig. 1. A block diagram of the functional components is presented in Fig. 1A. A wireless link established by magnetic induction between coils associated with the device and an external reader (that is, any NFC-enabled smartphone, tablet, etc.) enables power delivery to and data transmission from a bare die NFC platform (2.38 mm × 2.38 mm; thickness of ~100 μm) (fig. S1). This chip (SL13A, ams AG) monolithically integrates components for ISO 15693 logging logic, 8K-bit data storage, temperature sensing, analog-digital conversion (ADC; 10-bit resolution with a single input and 25-Hz sampling rate), and power management based on voltage rectification and stabilization. The latter provides dc power to the LED and to a photodetector and amplifier in a trans-impedance configuration (fig. S2 and table S1). The ADC digitizes the output of the photodetector, and the logging logic enables wireless data transmission. Images of a representative device (16 mm Ø) and its functional subsystems are presented in Fig. 1 (B to E). The interconnects (widths of 60 to 90 μm and thicknesses of 5 μm) adopt serpentine shapes in accordance with design rules in stretchable electronics. The circular loop antenna (inner and outer diameters of 1.2 and 1.6 cm, respectively) exploits 14 turns of copper lines with widths and thicknesses of ~70 and 5 μm, respectively (Fig. 1E). The antenna has an inductance and resistance of 5.9 microhenrys (μH) and 51 ohms at 13.56 MHz, respectively, and an equivalent Q factor of 9.8 (fig. S3A).

All metal traces include encapsulating layers of polyimide above and below to physically and electrically insulate the copper and to place it at the neutral mechanical plane. With thin elastomeric substrates and encapsulating layers, these optimized layouts enable system-level elastic responses to large strain deformations. In practice, finite element analysis (FEA) guides the selection of layouts for the NFC die and other chip-scale components, and the shapes and configurations of the serpentine interconnects (see the Supplementary Materials for more details). An iterative optimization process involves (i) identifying locations of strain concentrations in all components for various applied strains and implementing modifications in layout/geometry to reduce these strains and (ii) ascertaining potential entanglement of interconnects and contact between components during mechanical deformation and making adjustments in configuration to avoid such issues. These procedures in mechanical design are constrained, of course, by considerations in circuit design. The outcome in Fig. 1B corresponds to several such design iterations. The deformed device layouts for applied strains of 10, 20, and 30%, obtained by FEA and experiments, respectively, are shown in Fig. 1 (F and G). The distribution of the maximum principal strain is also shown in Fig. 1F. The elastic stretchability is ~10%, assuming a 0.3% yield strain for the copper. For 30% stretching, the maximum principal strain in copper is ~1.8% (in interconnects) and is much lower than the fracture strain (~5%) of copper. The device continues to function properly even when stretched up to 30% (fig. S4).

An exploded-view schematic illustration of a device mounted on the forearm is presented in Fig. 2A. Here, an ultrathin (~25 μm) medical adhesive (acrylic adhesive, Scapa Healthcare) bonds the device face down to the skin (Fig. 2B). The distance between the LED and the photodiode sets the characteristic depth associated with backscattered light that arrives at the photodiode. The device shown here uses a distance of 2.5 mm to yield depths that allow sufficient optical absorption by the blood and, at the same time, adequate signal levels for operation of the LED at modest current levels (~4 mA). These power levels can be provided by a standard, NFC-equipped smartphone (Galaxy Note 4, Samsung), as shown in Fig. 2C. The phase responses measured at different distances to the primary coil of up to 20 mm are shown in fig. S5A. The device, in practice, allows operation with a smartphone over distances of up to roughly 2 cm, even under deformation. Improved range is possible with high-power transmission systems.

Arterial pulse waves temporally modulate the backscattered light to provide important information on the hemodynamic status of the patient. The sampling rate, 25 Hz, which is enabled by the NFC chip used here, although modest when compared to conventional wired hardware, allows sufficient resolution for many purposes. For example, measured signals that correspond to 13 cardiac beat cycles are shown in Fig. 2D. The data reveal the systolic peak (that is, the maximum pressure generated by the systolic ejection) and the dicrotic notch, as highlighted in Fig. 2E. In this example, a second notch is also visible, likely because of multiple reflections associated with blood flow (18). Proper calibration of the device based on measurement of the diastolic and systolic pressure by a standard oscillometry technique yields estimates of the mean arterial pressure (MAP). The MAP can be calculated as $P_{diastolic} + 0.33 \times (P_{systolic} - P_{diastolic})$, which is roughly equivalent to the area under the arterial pressure curve, divided by the duration of the beat and averaged over several beats (19–21). In this manner, changes in MAP can be tracked by measuring the change in the maximum and minimum values of the pressure. Fourier analysis shows the different components of the signal (Fig. 2F), where the fundamental frequency corresponds to the heart rate (~90 beats per minute in this case). At the same time, the temperature of the skin can also be monitored wirelessly by using the internal temperature sensor associated with the NFC chip. Data indicate only minor changes in temperature during operation, with a peak of ~37°C (fig. S6).

Oximetry for peripheral vascular disease assessment

The addition of a red (625 nm, InGaAlP) LED to this platform allows quantitative measurement of tissue oxygenation and its temporal variations, which is important to monitor peripheral blood circulation. Here, an astable oscillator switches current flow between the red and IR LEDs at frequencies set by the R_1C_1 and R_2C_2 tanks, where R_1 and R_2 and C_1 and C_2 are the resistors and capacitors, respectively, that connect the LED to the bipolar transistors (Fig. 3, B and C, table S2, and movie S1). In this simple time-domain multiplexing strategy, backscattered amplitudes for both red and IR can be captured using a single photodetector and a trans-impedance amplifier identical to that of the previously described device. The rectangular loop antenna exploits five turns of copper lines with widths and thicknesses of 200 and 5 μm, respectively. The antenna has a size of 3.4 cm × 2.8 cm and exhibits an inductance and a resistance of 1.7 μH and 11 ohms at 13.56 MHz, respectively, resulting in a Q factor of 13.5 (fig. S3B). The larger size of this design compared to the circular one provides stronger coupling with the primary coil (fig. S5B). The switching currents, which bias the IR and red LEDs, corresponding to estimated power consumptions of 10 and 5 mW, respectively, are shown in fig. S7A. The total stretchability of this system, which is obtained from FEA, is larger than 30% (fig. S8) despite the increased complexity in electrical design. A
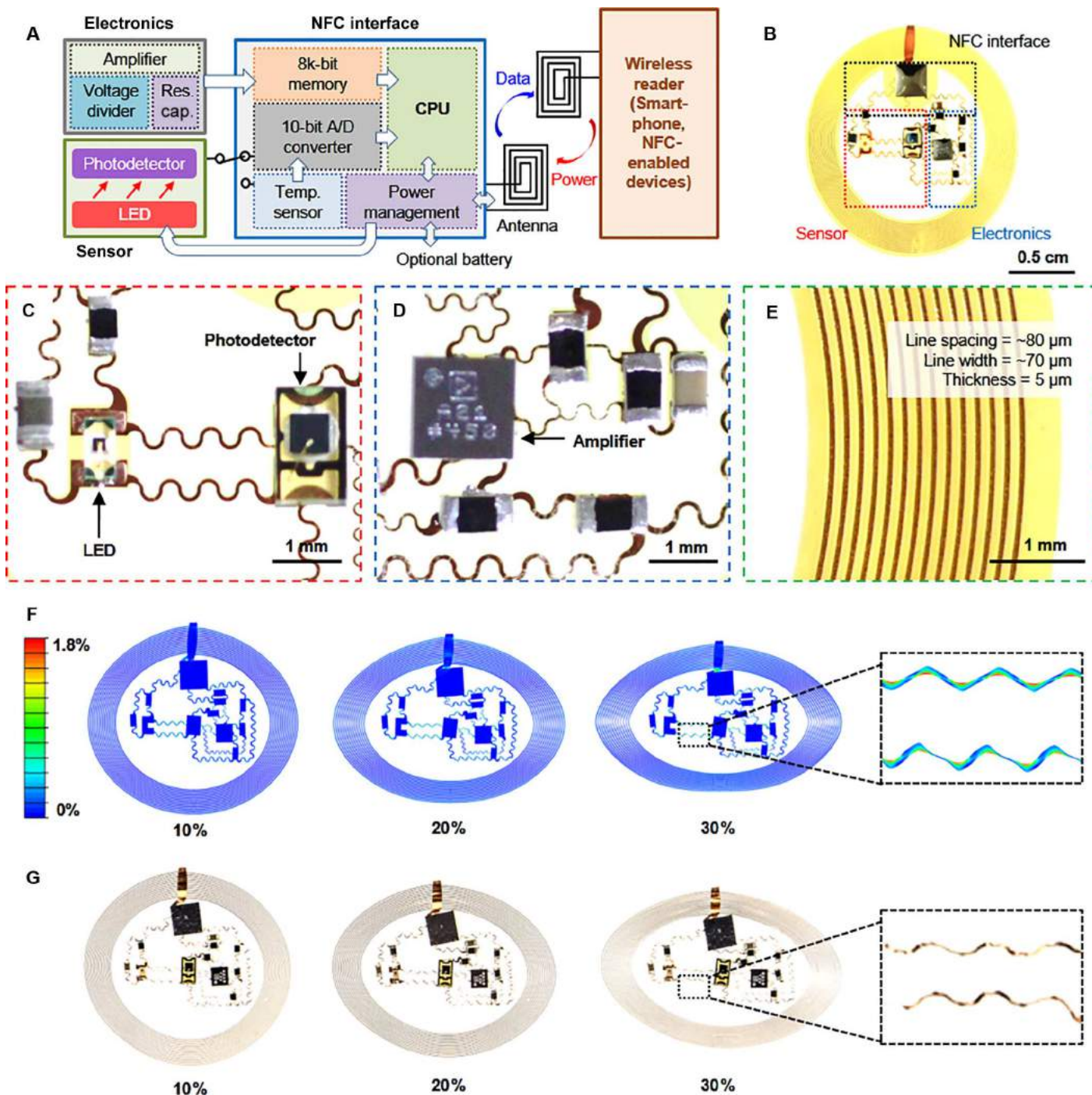
Fig. 1. Wireless epidermal optoelectronics. (**A**) Block diagram of the system, including its NFC wireless components for wireless power transfer and data communication. An external set of reader electronics delivers power to the device through magnetic inductive coupling. This power activates the optoelectronic components, the analog/digital (A/D) converter, and the NFC hardware for wireless transmission of the output of the photodetector back to the reader, where it is recorded for further processing. (**B**) Image of a complete device configured to measure heart rate. (**C** to **E**) Magnified sections of (B). The system includes an IR LED and a photodetector (C), an amplifier and resistors for conditioning (D), and an inductive coil (E). (**F**) FEA at the system level reveals the displacement and strain distributions for uniaxial strains up to 30%. (**G**) Corresponding images of the device. The inset highlights a highly deformed region for both modeling and experiment. The system functions properly even at the highest strains illustrated here.
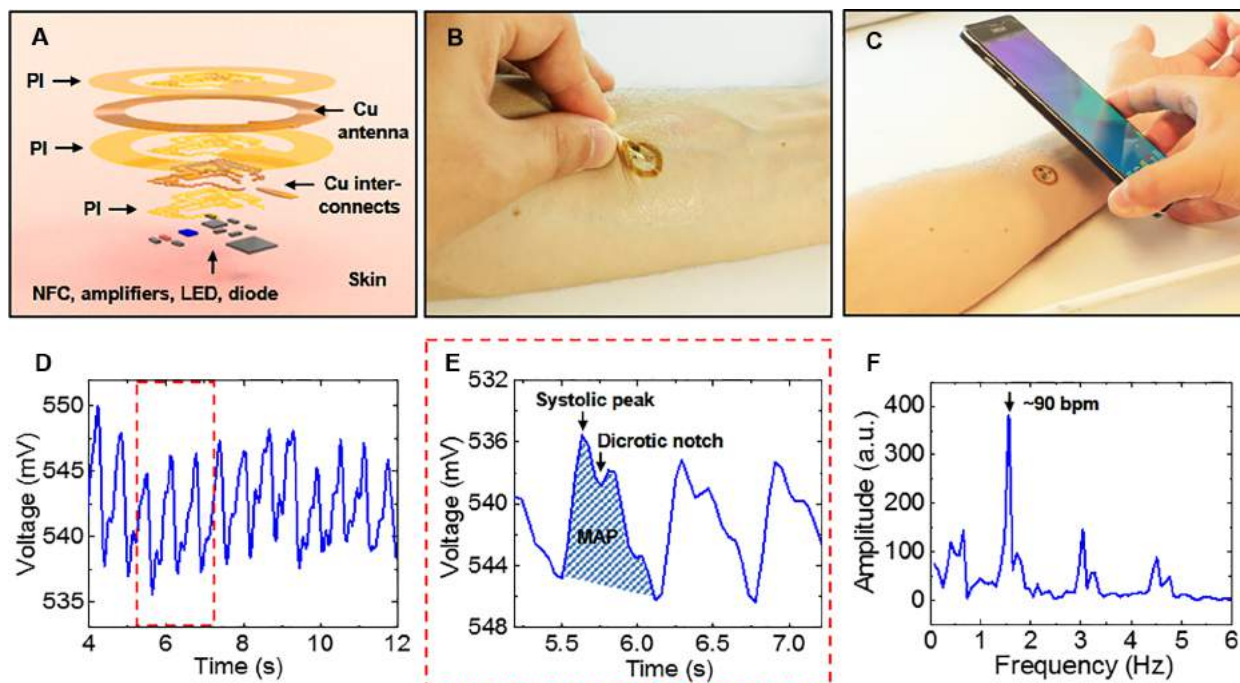
Fig. 2. Wireless epidermal optoelectronic system with a single LED and photodetector designed for heart rate and MAP tracking. (**A**) Exploded-view illustration of the device construction. (**B**) Image of a device mounted on the skin while deformed by pinching. (**C**) Image of the device during wireless operation with a smartphone, for both power deliver and data communication. (**D**) Wireless measurement results during recording on the forearm. (**E**) Magnified view of the red dashed box in (D), with an inverted y-axis scale, for ease of viewing. The systolic peak and the dicrotic notch, evident in these data, correspond to the maximum pressure generated during the systolic ejection and to the closing of the aorta, respectively. The MAP relates to the area under the pulse waveform. (**F**) Fourier transform of the signal in (D). The graphs show three harmonics, the first one of which corresponds to the beat rate (~1.5 Hz or 90 beats per minute).

black textile (22) coated with an ultrathin low-modulus (E = ~5 kPa) silicone elastomer (Silbione RT Gel 4717, Bluestar Silicones) serves as a robust, reusable substrate that facilitates soft adhesion to the skin and, at the same time, blocks external light that would otherwise interfere with the measurement (Fig. 3D). The output data are continuously collected without movement artifacts (fig. S9). Physical deformation of the device can affect the absolute values of the measured photoresponse. Nevertheless, the ratios of responses from multiple LEDs and the changes relative to a baseline value are largely invariant, as illustrated in the results in fig. S10.

A standard procedure to assess peripheral vascular diseases uses an inflating cuff placed around the bicep to occlude venous (but not arterial) blood flow (fig. S11). This procedure provides a means for in vivo evaluation of the device performance. Data captured wirelessly from the forearm using an NFC reader (AMS Inc.) at a distance of 0.7 cm for 240 s are shown in Fig. 3E, corresponding to 120 s of occlusion (highlighted in gray) with 60 s of rest and recovery before and after. A narrow temporal range appears in Fig. 3F. Extraction of the high- and low-voltage values allows separation of data corresponding to light from the IR and red LEDs, respectively. A low-pass filter (0.5 Hz, 10th-order Butterworth digital filter) eliminates high-frequency noise. Here, the slope of the baseline evaluated during the resting period (60 s) accounts for eventual drift, which is subtracted from the entire data set. Noise assessment of the device measured in vitro on a phantom device defines a resolution limit of 50 μM (more details can be found in Materials and Methods and in figs. S12 and S13). Variations in the

concentration of oxyhemoglobin (ΔO_2Hb) and deoxyhemoglobin (ΔHHb) follow the computed ratios of the photodetector responses during red and IR illumination, using standard procedures with a modified Beer-Lambert law (see Materials and Methods for more details). Results before, during, and immediately after venous occlusion, along with the total hemoglobin variation ($\Delta tHb = \Delta O_2Hb + \Delta HHb$) obtained with a standard, wired, bulk commercial oximeter (IMAgent) and the wireless epidermal device, are shown in Fig. 3 (G and H). The IMAgent oximeter uses laser diodes that emit at wavelengths of 830 and 690 nm, coupled to separate optical fibers for light delivery to the skin. A fiber bundle collects backscattered light and delivers it to photomultiplier tubes (PMTs) for detection. Additional details appear in the experimental section. Postprocessing of raw data obtained from the IMAgent and the epidermal devices yields separate in vivo oxygenation parameters for the period during the venous occlusion. Despite the differences between these two systems, that is, in the illumination conditions (noncollimated versus collimated light source) and in the detector configurations (bare die photodetector versus fiber bundle and PMT), the curves reveal similar trends and similar values for the variations in hemoglobin concentration. In a practical sense, the analysis of oxygenation is most straightforward when the system is located on a relatively flat surface of the body. Previous studies explored the dependence of the differential pathlength factors (DPFs) as a function of body location using frequency-domain or time-domain near-IR (NIR) systems. Analysis must use these location-specific DPFs. Alternatively, the system can be calibrated against a standard measurement. We note
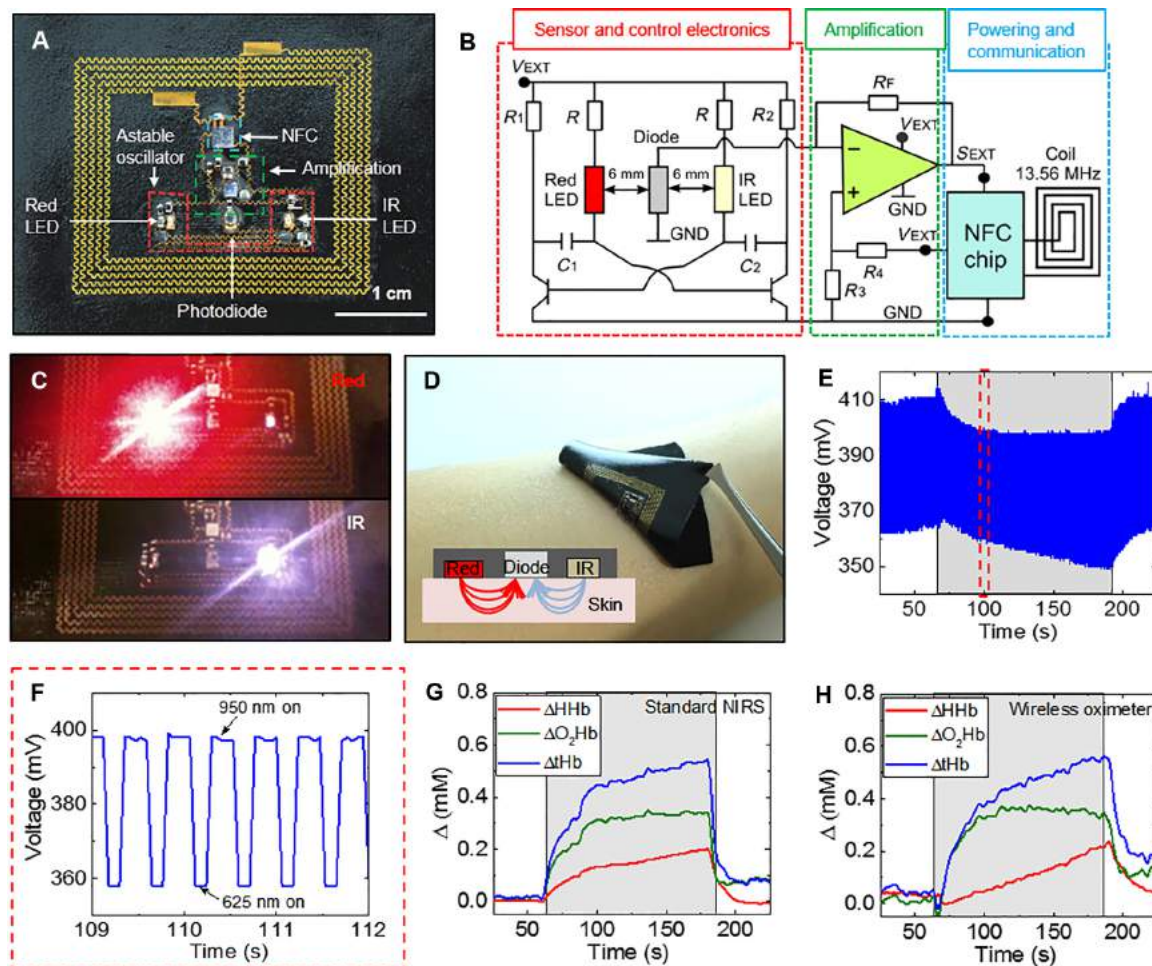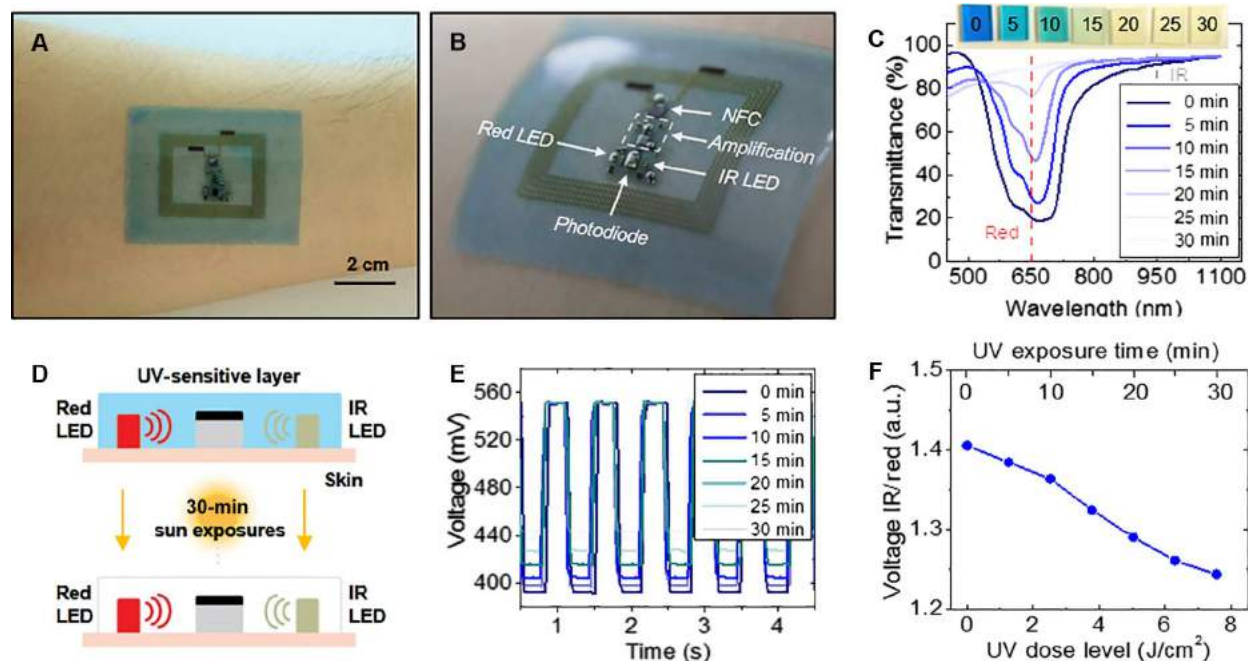
Fig. 3. Wireless epidermal optoelectronic system with two pulsed LEDs and a single photodetector to monitor peripheral vascular disease. (**A**) Image of an epidermal wireless oximeter that includes a red LED, an IR LED, a photodiode, and associated electronics all in a stretchable configuration mounted on a soft, black textile substrate coated with a low-modulus silicone elastomer. (**B**) Schematic illustration of the circuit of the device. An astable oscillator switches current between the two LEDs to allow time-multiplexed measurement of both wavelengths with a single photodetector. The R_1C_1 and R_2C_2 tanks set the frequency of the oscillator. GND, ground. (**C**) Images of the device operating during activation of the red LED (top) and the infrared LED (bottom). (**D**) Image of the device mounted on the forearm. (Inset) Schematic illustration of the operating principle. (**E**) Functional demonstration in a procedure that involves transient vein occlusion (gray box in the graph). An inflating cuff on participant's bicep temporarily occludes venous blood flow set to a pressure slightly below the arterial pressure (50 mmHg). (**F**) Magnified view of the red dashed box in (E). (**G** and **H**) Measurements obtained by a commercial oximeter and an epidermal device, simultaneously recorded from adjacent regions of the forearm. NIRS, NIR spectroscopy.

that skin coloration and body location can affect the overall signal levels, but not the ratios and, therefore, not the oxygenation.

UV dosimetry using color-responsive materials
In another use case, similar device platforms can interrogate changes in optical properties of materials designed to offer colorimetric responses to parameters of interest. As an example, a UV dosimeter can be constructed by coating a film that contains a UV-responsive dye (CR234-BT2B, Spectra Group Inc.) on top of a device similar to that in Fig. 3. A stretchable, epidermal system of this type (components listed in table S3) appears in Fig. 4 (A and B), where a thin layer of a transparent silicone elastomer (~300 μm) serves as the substrate and a UV-sensitive dye in a silicone matrix (~500 μm) covers the entire device. In this case, the dye changes from blue to transparent upon exposure to UV light,

where a dose of ~8 J/cm^2 causes a complete change (Fig. 4C). The working principle is illustrated in Fig. 4D. Here, both LEDs emit in a direction parallel to the plane of the device, such that the photodetector responds largely to the amount of light that passes through the UV-sensitive layer in an in-plane transmission mode. Representative measured signals are presented in Fig. 4E, where the high voltages (near 550 mV) and low voltages (near 400 mV) correspond to illumination by the red and IR LEDs, respectively. Consistent with the spectral characteristics of the dye, the transmittance in the red (640 nm) increases strongly with increasing UV dose, whereas that in the IR (950 nm) remains constant, such that the latter can be used as a reference. The ratio of the two signals (IR and red) defines a metric to determine the dose (Fig. 4F) in a manner that reduces sensitivity to external illumination conditions, wireless power delivery, and other

Fig. 4. Wireless epidermal optoelectronic system with two pulsed LEDs, a single photodetector, and a colorimetric responsive material designed for UV dosimetry. (**A** and **B**) Images of the device, which includes a red LED, an IR LED, and a photodiode, all encapsulated with thin, stretchable silicone film doped with a dye that changes color upon exposure to UV light. The two LEDs switch at different frequencies, through the use of an astable oscillator, to enable time-multiplexed readout with a single photodetector. (**C**) Optical transmittance of the UV-sensitive layer at different UV exposure dose levels, with corresponding images (the material changes from blue to transparent). (**D**) Sketch illustrating the operating principle. The LEDs emit light laterally through the UV-responsive layer. The use of one red and one IR LED enables differential measurement of the transmitted light. (**E** and **F**) Measurements at varying times of exposure to UV light from a solar simulator. The changes in transmission occur mainly at the red wavelength (640 nm), consistent with spectroscopic characterization of the material in (C). The ratio of the two signals is independent of both the power and the bias conditions of the LEDs. a.u., arbitrary units.

effects. This type of dosimetry cannot be easily replicated with an approach that relies on a conventional UV photodetector. A simplified version can be constructed with only one LED (red) using designs similar to those for pulse monitoring (Figs. 1 and 2). The performance of such a system appears in fig. S12.

Four-color skin spectrometer

Extensions of these concepts can support basic spectrometer functionality in a stretchable, epidermal format. An example of a device that involves design concepts, materials, and components similar to those of the other platforms is shown in Fig. 5A, but with four different LEDs (IR, red, orange, and yellow) and time-domain multiplexed measurement using a single photodetector at a distance of 1 mm from each LED (fig. S13). This platform allows for color measurement, which is relevant for applications ranging from the evaluation of food products to skin tone. The system involves pairwise switching of the LEDs. Specifically, the red and IR LEDs switch at low frequency, whereas the orange and yellow LEDs switch at a comparatively high frequency, as illustrated in Fig. 5B, fig. S13, and movie S2. The induced currents through each LED during this switching process are shown in fig. S7B. The IR LED is on for ~2 s and off for ~1 s. The orange LED is on for ~0.7 s and off for ~0.4 s. The red and yellow LEDs are on when the others are off. Two separate astable oscillators control the switching. The structural details and switching mechanisms are summarized in fig. S13, and the values of all components

are included in table S4. The device can also function properly even when completely submerged in water because of the water barrier properties of the encapsulating layers and the low absorption losses associated with radio frequency operation in the NFC band (Fig. 5C and movie S3). Measured and computed phase responses from devices in air, on skin, and immersed in water are shown in fig. S14. The results are similar in these cases.

A simple functional demonstration involves measurements of the optical reflectance of apples with three different colors (red, yellow, and green). Data collected using a UV-Vis-NIR spectrophotometer (Cary 5000, Agilent) appear in Fig. 5D, where the vertical lines denote the wavelengths of the LEDs. Among them, the yellow apple has the highest reflectance (~60%) and the red apple has the lowest reflectance (~25, ~15, and ~10%) at red, orange, and yellow wavelengths. The reflectance in the IR is similar. Data collected for 30 s for each case are presented in Fig. 5E, with the wireless device conformally mounted on the surfaces of the apples. To extract the reflectance value at each LED wavelength from the various measured ratios, it is necessary to perform a separate measurement with only the illumination from the red LED using a simplified version of the device. More details on the analysis can be found in the experimental section. The calculated reflectance at each LED wavelength is presented in Fig. 5F. These outcomes are consistent with spectra separately recorded with a conventional spectrometer, as in Fig. 5D. The same measurement and analysis procedures can capture the optical characteristics of samples of polydimethylsiloxane

Kim *et al. Sci. Adv.* 2016;2:e1600418   3 August 2016

6 of 10
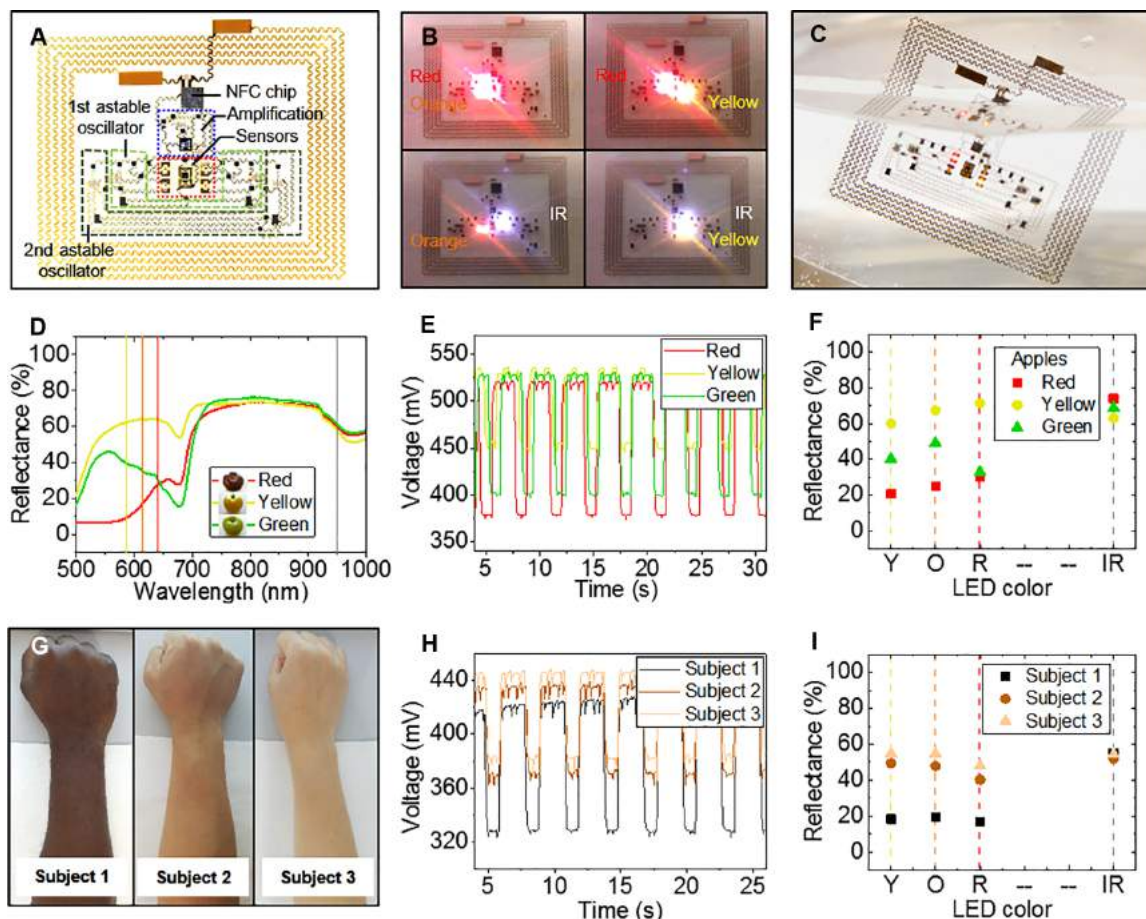
Fig. 5. Wireless epidermal optoelectronic system with four pulsed LEDs and a single photodetector for spectrophotometric characterization. (**A**) Image of a wireless spectrometer that includes four pulsed LEDs, each with a different color (red, IR, orange, and yellow). There are two switching LED pairs in the device (red-IR and yellow-orange). Two astable oscillators control the switching at four different frequencies to distinguish each signal. (**B**) Images of the device operating while the LEDs are activated. (**C**) Image of a device operating while submerged in water captured at a moment during activation of red and yellow LEDs. (**D**) Reflectance measurement of three different colored apples. The vertical lines denote the wavelength of each LED light. (**E**) Wireless measurement of three different colored apples. (**F**) Calculated reflectance from measurement data of apples with different colors. (**G**) Images of subjects with different skin colors. (**H**) Wireless measurement data of skins with varying colors. (**I**) Calculated reflectance from the measurement data of skins with different colors.

(PDMS) dyed to different colors (white, yellow, orange, light red, red, green, and purple). The results correspond well with separately recorded spectra (fig. S15). The reflectance of the white PDMS block serves as a baseline for normalization.

The assessment of skin color with these epidermal devices represents an application of relevance to detect various diseases. A notable example is in jaundice in newborns, where high levels of bilirubin in the blood yield yellowish coloration of the skin (23). The potential toxicity associated with bilirubin demands monitoring to identify cases of hyperbilirubinemia, acute bilirubin encephalopathy, or kernicterus (24, 25). Jaundice in adults is also associated with liver disease, where bronzing of the skin in patients with diabetes can indicate defects in iron metabolism with the possibility of liver failure, known as hemochromatosis (26, 27). Noticeable darkening of the skin often accompanies the development of adrenal diseases, such as Addison's disease (28). As an example of the utility in such contexts, devices laminated onto the forearms of different volunteers allow determination of skin

color, as shown in Fig. 5G. The results of the experiment and the calculated reflectance of each subject, respectively, are reported in Fig. 5 (H and I). The red, orange, and yellow wavelengths are sensitive to skin color, whereas the IR is not, which is expected because of the strong absorption of oxygenated hemoglobin at this wavelength. Overall, lighter skin reflects more light than darker skin, consistent with the data in Fig. 5H. As expected, the calculated reflectance values of the subjects increase from subjects 1 to 3 (Fig. 5I).

DISCUSSION

The devices presented here provide battery-free, fully wireless optoelectronic functionality in physical forms that have properties compatible with the epidermis to allow intimate integration with the skin for acquisition of various health information. An attractive feature of the NFC approach is its ability to enable both wireless power delivery to and

extraction of data from the devices in a manner that is compatible with smartphones and other consumer electronics. The battery-free operation allows the systems to be engineered in much thinner, lighter, and more wearable formats than would otherwise be possible. The data from device examples reported here provide information on heart rate and temporal dynamics of blood flow, tissue oxygenation, and color of the skin. The addition of color-responsive materials expands the functionality to allow sensing not only of the skin but also of key environmental parameters, as demonstrated in UV dosimetry. This type of active spectrophotometry can significantly expand the function in wearable device technologies, with additional future possibilities for use within the body.

MATERIALS AND METHODS

Fabrication of the coils and interconnects
A Cu foil (5 μm thick, Oak Mitsui MicroThin Series) provided the material for the coil. A film of polyimide (PI; 2.4 μm thick, PI2545, HD Microsystems) spin-casted onto the Cu foil at 2000 rpm for 30 s and baked on a hot plate at 150°C for 5 min and in a vacuum oven at 250°C for 75 min formed an insulating layer coating. Laminating this PI-coated Cu foil onto the PDMS (10:1, Sylgard 184)–coated glass slide, with the PI side down, allowed patterning of the Cu foil into a coil geometry by photolithography (photoresist AZ 4620; spin-casting at 3000 rpm for 30 s, baking on a hot plate at 110°C for 3 min, UV irradiance for 300 mJ·cm^{-2}, and development for ~40 s with developer AZ 400K/deionized water solution of 1:2 volume ratio), and wet etching (CE-100 copper etchant, Transense; ~2 min with frequent rinsing by water). A coating of PI spin-cast at 2000 rpm for 30 s covered the coil formed in this way. Photolithography (AZ 4620) and oxygen plasma etching (200 mtorr, 20 sccm O_2, 150 W for 900 s) created via holes through the PI. Oxide remover (Flux, Worthington) eliminated the copper oxide on the pads exposed at the base regions of the via holes. Electron beam evaporation of Cu (1 μm thick) followed by photolithography (AZ 4620) and wet etching (copper etchant) defined a pattern of interconnects. Spin casting yielded another 2.4-μm-thick layer of PI over the entire patterns. Electron beam evaporation of a 50-nm-thick layer of SiO_2 followed by photolithography (AZ 4620) and reactive ion etching (50 mtorr, 40 sccm CF_4, 100 W for 10 min) created a hard mask for removal of the PI by oxygen plasma etching in all regions except for those above the traces for the coil and interconnects.

NFC die and other chip-scale components (LEDs, photodetector, and amplifier)
An SL13A (ams AG, ISO/IEC 15693; input capacitance of 25 pF) bare die chip served as the NFC platform. In addition to 8K-bit memory and an internal temperature sensor, the chip also supports a 10-bit ADC with a single analog input and energy-harvesting capabilities for a rectified and stabilized output voltage (3.4 V). The maximum power that can be delivered to the external circuitry is about 12 mW, depending on the coupling efficiency. The maximum sampling rate for reliable operation of the ADC is ~25 Hz, and the input range is 300 to 600 mV. Polishing reduced the thickness of the die to <100 μm thick. Information on the LEDs, the photodetector, and the amplifier are as follows: IR LED: SFH 4043, 950 nm, 1 mm × 0.5 mm × 0.45 mm, Osram Opto Semiconductor; red LED: LR QH9F, 625 nm, 1 mm × 0.5 mm × 0.35 mm, Osram Opto Semiconductor; orange LED:

APG1005SEC-T, 611 nm, 1 mm × 0.5 mm × 0.2 mm, Kingbright Electronic Co.; yellow LED: APG1005SYC-T, 591 nm, 1 mm × 0.5 mm × 0.2 mm, Kingbright Electronic Co.; photodetector: EMD7000X01, 2 mm × 1.25 mm × 0.85 mm, Vishay Semiconductors; amplifier: ADA4505-2, 1.42 mm × 1.42 mm × 0.6 mm, Analog Devices Inc.

Transfer and assembly
A cellulose-based water-soluble tape (Grainger) allowed retrieval of the coils and interconnect traces from the temporary support used for processing and their delivery onto the device substrate.

Heart rate and temporal dynamics of arterial blood flow. An ultrathin (~25 μm) medical adhesive (acrylic adhesive, Scapa Healthcare) served as a means to bond the devices to the skin, much like a temporary tattoo. A thin layer of a silicone elastomer (Q1-4010, Dow Corning) provided an encapsulating layer.

Oximetry for peripheral assessment. A black textile substrate blocked the environmental light. An ultrathin low-modulus silicone elastomer coating (Silbione) yielded a modest level of adhesive strength to facilitate reuse. An astable oscillator controls the current in the LEDs. This oscillator combines a resistance-capacitance tank with a bipolar transistor (BC847BMB, NXP Semiconductors).

UV dosimetry using color-responsive materials. A thin layer of silicone (PDMS, Sylgard 184; ~300 μm) served as a substrate (300 μm) and a matrix material for the UV sensing layer (~500 μm). An electronic circuit similar to that used for the oximeter provides data amplification and conditioning. The distance between the LEDs and the photodiode is 1 mm, which is selected to maximize the signal level.

Four-color skin spectrometer. A thin layer (~500 μm) of silicone elastomer (Ecoflex, Smooth-On; E = 60 kPa) served as a substrate. An ultrathin low-modulus silicone elastomer (Silbione) spin-coated on top of the device promoted adhesion to target objects and provided encapsulation. Here, two astable oscillators switched the current in the LEDs at four different frequencies set by four RC tanks. Complete electrical schematics and details of the components are in the Supplementary Materials.

For the blood oximetry, the UV dosimetry, and the four-color skin spectrometer, the rectangular coil was used to ensure higher coupling efficiency. In this case, a capacitor of 51 pF was added in parallel to the coil to tune the resonance near 13.56 MHz.

Dissolution of the water-soluble tape completed the transfer. Thinned NFC die and components (LEDs, photodetector, amplifier, resistors, and capacitors) were attached to the interconnect patterns by a modified flip-chip bonding method with an indium/Ag-based solder paste (Indalloy 290, Indium Corporation; ≈165°C for 2 min in a reflow oven).

NIR spectroscopy system for oximeter benchmarking
Measurements using a commercial frequency-domain oximeter (Imagent; ISS Inc.) established comparative data to determine the performance of the devices reported here. This commercial tool uses laser diodes to generate modulated light (110 MHz) at 830 and 690 nm and uses source time-multiplexing (maximum amplitude: 10 mW; mean amplitude after multiplexing: 1 mW). A pair of optical fibers (400-μm hard plastic-clad glass) delivers light to the skin. A fiber bundle (3 mm in diameter) captures the backscattered light and transmits it to PMTs for heterodyne detection to yield a cross-correlation signal that is captured by an ADC. Fast Fourier transform of the cross-correlation signal yields the average intensity, modulated intensity, and relative

phase. The data used here corresponded to average intensity values sampled at 25 Hz.

In vitro oximeter noise measurements

Measurements of the noise involved a sensor located on a side of a cubic phantom (100 mm × 100 mm × 100 mm) designed to reproduce basic optical properties of biological tissue [absorption coefficient (μ_a) = 0.0093 mm^{-1} and reduced scattering coefficient (μ_s') = 1.05 mm^{-1} at 620 nm; μ_a = 0.01 mm^{-1} and μ_s' = 0.95 mm^{-1} at 950 nm]. Separating high- and low-voltage values from the raw signal yielded measurements at the two wavelengths of the LEDs. The SD of these data defined the noise as ~1% at 950 nm and ~2.5% at 620 nm for an acquisition time of 120 s (fig. S16). An estimate of the instrument sensitivity to changes in oxygenation followed the application of the modified Beer-Lambert law to the data. The DPF was computed for each wavelength based on known absorption and reduced scattering coefficient (*29*) as follows: $1/2\sqrt{3\mu_s'/\mu_a}$. In this way, the SDs in the measured data corresponded to uncertainties in the concentration of ~0.050 mM for both oxygenated and deoxygenated hemoglobin (fig. S17).

A similar analysis revealed corresponding properties for the commercial instrument. Signal variability was 0.24% at 830 nm and 0.1% at 690 nm, corresponding to a concentration uncertainty of ~0.0050 mM for both oxygenated and deoxygenated hemoglobin.

Oximeter electrical in vivo measurements

Venous occlusion procedures were used for in vivo testing. Measurements involved a wireless device and a homemade single-channel optical probe (6-mm source-detector distance) connected to the commercial system positioned close to one another on the forearm. An inflating cuff placed around the bicep occluded venous blood flow at a pressure set above venous but below arterial pressure (50 mmHg). Before testing, the subject was comfortably seated and allowed to adjust to the environment for 120 s. Data were acquired synchronously on the two optical systems for 240 s, corresponding to 120 s of occlusion with 60 s of rest and recovery before and after. An NFC reader (ams) was used for data acquisition at distances of ~7 mm.

Oximeter data analysis

Analysis of data from the reported devices and the commercial system allowed extraction of oxygenation parameters. Separating high- and low-voltage values from the raw signal from the wireless devices yielded data for the two optical wavelengths. Optical densities (ODs), defined as

$$OD = -\ln[I(t)/I_o] \qquad (1)$$

where $I(t)$ is the time dependence of the light intensity and I_o is its initial value, were computed for both oximeters. Postprocessing involved a low-pass filter at 0.5 Hz with a 10th-order Butterworth digital filter and subtraction of any slow drift in the baseline. Variations in the concentration of oxyhemoglobin and deoxyhemoglobin followed from application of the modified Beer-Lambert law for the two recordings

$$\begin{bmatrix} \Delta O_2 Hb \\ \Delta HHb \end{bmatrix} = \frac{1}{\rho} \begin{bmatrix} \varepsilon_{O_2Hb}(\lambda_1) & \varepsilon_{HHb}(\lambda_1) \\ \varepsilon_{O_2Hb}(\lambda_2) & \varepsilon_{HHb}(\lambda_2) \end{bmatrix} \\ \times \begin{bmatrix} DPF^{-1}(\lambda_1) & 0 \\ 0 & DPF^{-1}(\lambda_2) \end{bmatrix} \begin{bmatrix} OD(\lambda_1) \\ OD(\lambda_2) \end{bmatrix} \qquad (2)$$

where $\Delta O_2 Hb$ and ΔHHb represent the changes in oxyhemoglobin and deoxyhemoglobin concentration, respectively; ρ is the interoptode distance; and ε and DPF are the exciton coefficients for the two chromophores and the DPF at these wavelengths, respectively. The extinction coefficients of the two forms of hemoglobin at the different wavelengths were obtained from Zijlstra *et al.* (*30*) ($\varepsilon_{O2Hb,640nm}$ = 0.011 mm^{-1}, $\varepsilon_{HbO,950nm}$ = 0.028 mm^{-1}, $\varepsilon_{HHb,640nm}$ = 0.106 mm^{-1}, $\varepsilon_{HHb,950nm}$ = 0.018 mm^{-1}, $\varepsilon_{O2Hb,690nm}$ = 0.0096 mm^{-1}, $\varepsilon_{O2Hb,830nm}$ = 0.021 mm^{-1}, $\varepsilon_{HHb,690nm}$ = 0.05 mm^{-1}, and $\varepsilon_{HHb,830nm}$ = 0.017 mm^{-1}). The DPFs were derived from Scholkmann and Wolf (*31*) (DPF$_{620nm}$ = 7, DPF$_{950nm}$ = 4.6, DPF$_{690nm}$ = 6.5, and DPF$_{830nm}$ = 5.5). The total hemoglobin variation was computed from the sum of the two forms of hemoglobin.

UV-sensitive layer and UV exposure

The UV-sensitive material consisted of a mixture of a UV-bleachable ink (CR234-BT2B, Spectra Group Inc.) with PDMS (part A/part B = 10:1; Sylgard 184, Dow Corning) at a weight ratio of 1:20 that offers a color change from blue to clear upon exposure to UV light. Hydrogen gas and air in the ink were removed after mixing under vacuum. Spin casting formed a blue UV–sensitive layer over the entire device. UV exposure was carried out with solar simulator (Oriel Sol1A model 94041A, Newport; UV intensity is 42 W/m^2) for 5, 10, 15, 20, 25, and 30 min (corresponding to 1.26, 2.52, 3.78, 5.04, 6.30, and 7.56 J/cm^2, respectively). Transmission spectra from 400 to 1100 nm were captured using a conventional spectrophotometer (Cary G5, Agilent) with air as the baseline without an integrating sphere.

Spectrometer reflectance calculation

The spectrometer involves two LED pairs (IR and red, and orange and yellow) that switch at low and high frequencies. Two different LEDs turn on at the same time upon device activation (IR and orange, IR and yellow, red and orange, and red and yellow). The photodetector collects reflected light associated with the operating pair. The voltage (V_{a+b}) output of the photodetector due to operation of two LEDs (designated as a and b) can be expressed as

$$V_{a+b} - v_0 = (i_a + i_b)R_F \qquad (3)$$

where i_a and i_b are the photocurrents associated with the two LEDs. The reflected/backscattered light is proportional to the measured photocurrent i_x. The photocurrent ($i_a + i_b$) from two LEDs can only be obtained by the measurement; however, the current (i_a) for only one LED cannot be acquired. Obtaining the reflectance at each LED wavelength required separate measurements with a different device to provide the value at the wavelength of the red LED. The current (i_{red}) measured in this way allowed calculation of the other current values from the measured ratios. All calculated reflectance values were normalized to allow straightforward comparison to those measured by the spectrophotometer.

SUPPLEMENTARY MATERIALS

Supplementary material for this article is available at http://advances.sciencemag.org/cgi/content/full/2/8/e1600418/DC1

note S1. Fabrication procedure for devices.
note S2. FEA and optimization of device layout.
fig. S1. Size and thickness of the AMS SL13A NFC chip.

fig. S2. Circuit diagram of the pulse rate monitoring device and an image of the device mounted on the forearm.

fig. S3. Coil characterization.

fig. S4. Device functionality.

fig. S5. Inductive coupling for various operating distances between the primary and secondary coil.

fig. S6. Temperature change during operation.

fig. S7. Current measurement of each LED during switching.

fig. S8. The distribution of maximum principal strain in the copper layer of the deformed oximeter device.

fig. S9. Data captured wirelessly from the forearm during up-and-down arm movement.

fig. S10. Data captured wirelessly from the forearm during deformation.

fig. S11. Wireless device benchmarked against a commercial NIR spectroscopy system.

fig. S12. UV dosimeter with one LED.

fig. S13. Four-color spectrometer.

fig. S14. Electromagnetic properties with different media.

fig. S15. Colored PDMS measurement using the four-color spectrometer.

fig. S16. Noise OD of the oximeter.

fig. S17. Ultimate concentration resolution of HHb and O_2Hb.

table S1. Values of the components used in the device for heart rate monitoring.

table S2. Values of the components used in the oximeter.

table S3. Values of the components used in the device for the UV dosimeter.

table S4. Values of the components used in the device for the four-color spectrometer.

movie S1. A movie of switching LEDs during the blood oximeter device operation.

movie S2. A movie of switching LEDs during the four-color spectrometer device operation.

movie S3. A movie of switching LEDs during the four-color spectrometer device operation in water.

REFERENCES AND NOTES

1. S. R. Steinhubl, E. D. Muse, E. J. Topol, The emerging field of mobile health. *Sci. Transl. Med.* **7**, 283rv3 (2015).
2. E. Monton, J. F. Hernandez, J. M. Blasco, T. Hervé, J. Micallef, I. Grech, A. Brincat, V. Traver, Body area network for wireless patient monitoring. *IET Commun.* **2**, 215–222 (2008).
3. S. A. Boppart, R. Richards-Kortum, Point-of-care and point-of-procedure optical imaging technologies for primary care and global health. *Sci. Transl. Med.* **6**, 253rv2 (2014).
4. C. Otto, A. Milenković, C. Sanders, E. Jovanov, System architecture of a wireless body area sensor network for ubiquitous health monitoring. *J. Mobile Multimedia* **1**, 307–326 (2006).
5. E. Jovanov, A. Milenkovic, C. Otto, P. C. de Groen, A wireless body area network of intelligent motion sensors for computer assisted physical rehabilitation. *J. Neuroeng. Rehabil.* **2**, 6 (2005).
6. R. C. Webb, Y. Ma, S. Krishnan, Y. Li, S. Yoon, X. Guo, X. Feng, Y. Shi, M. Seidel, N. H. Cho, J. Kurniawan, J. Ahad, N. Sheth, J. Kim, J. G. Taylor VI, T. Darlington, K. Chang, W. Huang, J. Ayers, A. Gruebele, R. M. Pielak, M. J. Slepian, Y. Huang, A. M. Gorbach, J. A. Rogers, Epidermal devices for noninvasive, precise, and continuous mapping of macrovascular and microvascular blood flow. *Sci. Adv.* **1**, e1500701 (2015).
7. D.-H. Kim, N. S. Lu, R. Ma, Y.-S. Kim, R.-H. Kim, S. Wang, J. Wu, S. M. Won, H. Tao, A. Islam, K. J. Yu, T.-i. Kim, R. Chowdhury, M. Ying, L. Xu, M. Li, H.-J. Chung, H. Keum, M. McCormick, P. Liu, Y.-W. Zhang, F. G. Omenetto, Y. G. Huang, T. Coleman, J. A. Rogers, Epidermal electronics. *Science* **333**, 838–843 (2011).
8. R. C. Webb, A. P. Bonifas, A. Behnaz, Y. Zhang, K. J. Yu, H. Cheng, M. Shi, Z. Bian, Z. Liu, Y.-S. Kim, W.-H. Yeo, J. S. Park, J. Song, Y. Li, Y. Huang, A. M. Gorbach, J. A. Rogers, Ultrathin conformal devices for precise and continuous thermal characterization of human skin. *Nat. Mater.* **12**, 938–944 (2013).
9. C. Dagdeviren, Y. Shi, P. Joe, R. Ghaffari, G. Balooch, K. Usgaonkar, O. Gur, P. L. Tran, J. R. Crosby, M. Meyer, Y. W. Su, R. C. Webb, A. S. Tedesco, M. J. Slepian, Y. G. Huang, J. A. Rogers, Conformal piezoelectric systems for clinical and experimental characterization of soft tissue biomechanics. *Nat. Mater.* **14**, 728–736 (2015).
10. J. Kim, A. Banks, H. Cheng, Z. Xie, S. Xu, K.-I. Jang, J. W. Lee, Z. Liu, P. Gutruf, X. Huang, P. Wei, F. Liu, K. Li, M. Dalal, R. Ghaffari, Y. Huang, S. Gupta, U. Paik, J. A. Rogers, Epidermal electronics with advanced capabilities in near-field communication. *Small* **11**, 906–912 (2015).
11. J. Kim, A. Banks, Z. Xie, S. Y. Heo, P. Gutruf, J. W. Lee, S. Xu, K.-I. Jang, F. Liu, G. Brown, J. Choi, J. H. Kim, X. Feng, Y. Huang, U. Paik, J. A. Rogers, Miniaturized flexible electronic systems with wireless power and near-field communication capabilities. *Adv. Funct. Mater.* **25**, 4761–4767 (2015).
12. S. Xu, Y. Zhang, L. Jia, K. E. Mathewson, K.-I. Jang, J. Kim, H. Fu, X. Huang, P. Chava, R. Wang, S. Bhole, L. Wang, Y. J. Na, Y. Guan, M. Flavin, Z. Han, Y. Huang, J. A. Rogers, Soft microfluidic assemblies of sensors, circuits, and radios for the skin. *Science* **344**, 70–74 (2014).
13. D. P. Rose, M. E. Ratterman, D. K. Griffin, L. Hou, N. Kelley-Loughnane, R. R. Naik, J. A. Hagen, I. Papautsky, J. C. Heikenfeld, Adhesive RFID sensor patch for monitoring of sweat electrolytes. *IEEE Trans. Biomed. Eng.* **62**, 1457–1465 (2015).
14. C. M. Lochner, Y. Khan, A. Pierre, A. C. Arias, All-organic optoelectronic sensor for pulse oximetry. *Nat. Commun.* **5**, 5745 (2014).
15. C. Zysset, N. Nasseri, L. Büthe, N. Münzenrieder, T. Kinkeldei, L. Petti, S. Kleiser, G. A. Salvatore, M. Wolf, G. Tröster, Textile integrated sensors and actuators for near-infrared spectroscopy. *Opt. Express* **21**, 3213–3224 (2013).
16. M. Krehel, M. Wolf, L. F. Boesel, R. M. Rossi, G.-L. Bona, L. J. Scherer, Development of a luminous textile for reflective pulse oximetry measurements. *Biomed. Opt. Express* **5**, 2537–2547 (2014).
17. M. Rothmaier, B. Selm, S. Spichtig, D. Haensse, M. Wolf, Photonic textiles for pulse oximetry. *Opt. Express* **16**, 12973–12986 (2008).
18. W. W. Nichols, S. J. Denardo, I. B. Wilkinson, C. M. McEniery, J. Cockcroft, M. F. O'Rourke, Effects of arterial stiffness, pulse wave velocity, and wave reflections on the central aortic pressure waveform. *J. Clin. Hypertens.* **10**, 295–303 (2008)
19. K. J. Kimble, R. A. Darnall Jr., M. Yelderman, R. L. Ariagno, A. K. Ream, An automated oscillometric technique for estimating mean arterial pressure in critically ill newborns. *Anesthesiology* **54**, 423–425 (1981).
20. W. H. Lewis, The evolution of clinical sphygmomanometry. *Bull. N. Y. Acad. Med.* **17**, 871–881 (1941).
21. K. Yamakoshi, H. Shimazu, M. Shibata, A. Kamiya, New oscillometric method for indirect measurement of systolic and mean arterial pressure in the human finger. Part 1: Model experiment. *Med. Biol. Eng. Comput.* **20**, 307–313 (1982).
22. K.-I. Jang, S. Y. Han, S. Xu, K. E. Mathewson, Y. Zhang, J.-W. Jeong, G.-T. Kim, R. C. Webb, J. W. Lee, T. J. Dawidczyk, R. H. Kim, Y. M. Song, W.-H. Yeo, S. Kim, H. Cheng, S. I. Rhee, J. Chung, B. Kim, H. U. Chung, D. Lee, Y. Yang, M. Cho, J. G. Gaspar, R. Carbonari, M. Fabiani, G. Gratton, Y. Huang, J. A. Rogers, Rugged and breathable forms of stretchable electronics with adherent composite substrates for transcutaneous monitoring. *Nat. Commun.* **5**, 4779 (2014).
23. M. L. Porter, B. L. Dennis, Hyperbilirubinemia in the term newborn. *Am. Fam. Physician* **65**, 599–606 (2002).
24. T. B. Newman, M. J. Maisels, Evaluation and treatment of jaundice in the term newborn: A kinder, gentler approach. *Pediatrics* **89**, 809–818 (1992).
25. American Academy of Pediatrics Subcommittee on Hyperbilirubinemia, Management of hyperbilirubinemia in the newborn infant 35 or more weeks of gestation. *Pediatrics* **114**, 297–316 (2004).
26. M. Awai, M. Narasaki, Y. Yamanoi, S. Seno, Induction of diabetes in animals by parenteral administration of ferric nitrilotriacetate. A model of experimental hemochromatosis. *Am. J. Pathol.* **95**, 663–673 (1979).
27. I. W. Dymock, J. Cassar, D. A. Pyke, W. G. Oakley, R. Williams, Observations on the pathogenesis, complications and treatment of diabetes in 115 cases of haemochromatosis. *Am. J. Med.* **52**, 203–210 (1972).
28. S. Ten, M. New, N. Maclaren, Addison's disease 2001. *J. Clin. Endocrinol. Metab.* **86**, 2909–2922 (2001).
29. S. Fantini, M. A. Franceschini, E. Gratton, D. Hueber, W. Rosenfeld, D. Maulik, P. G. Stubblefield, M. R. Stankovic, Non-invasive optical mapping of the piglet brain in real time. *Opt. Express* **4**, 308–314 (1999).
30. W. G. Zijlstra, A. Buursma, W. P. Meeuwsen-van der Roest, Absorption spectra of human fetal and adult oxyhemoglobin, de-oxyhemoglobin, carboxyhemoglobin, and methemoglobin. *Clin. Chem.* **37**, 1633–1638 (1991).
31. F. Scholkmann, M. Wolf, General equation for the differential pathlength factor of the frontal human head depending on wavelength and age. *J. Biomed. Opt.* **18**, 105004 (2013).

Kim *et al. Sci. Adv.* 2016;**2**:e1600418   3 August 2016

10 of 10

The following resources related to this article are available online at http://advances.sciencemag.org. (This information is current as of August 11, 2016):

Updated information and services, including high-resolution figures, can be found in the online version of this article at:
http://advances.sciencemag.org/content/2/8/e1600418.full

Supporting Online Material can be found at:
http://advances.sciencemag.org/content/suppl/2016/08/01/2.8.e1600418.DC1

This article **cites 31 articles,** 8 of which you can access for free at:
http://advances.sciencemag.org/content/2/8/e1600418#BIBL

Supplementary Materials for

Battery-free, stretchable optoelectronic systems for wireless optical characterization of the skin

Jeonghyun Kim, Giovanni A. Salvatore, Hitoshi Araki, Antonio M. Chiarelli, Zhaoqian Xie,
Anthony Banks, Xing Sheng, Yuhao Liu, Jung Woo Lee, Kyung-In Jang, Seung Yun Heo,
Kyoungyeon Cho, Hongying Luo, Benjamin Zimmerman, Joonhee Kim, Lingqing Yan, Xue Feng,
Sheng Xu, Monica Fabiani, Gabriele Gratton, Yonggang Huang, Ungyu Paik, John A. Rogers

The PDF file includes:

- fig. S16. Noise OD of the oximeter.
- fig. S17. Ultimate concentration resolution of HHb and O_2Hb.
- table S1. Values of the components used in the device for heart rate monitoring.
- table S2. Values of the components used in the oximeter.
- table S3. Values of the components used in the device for the UV dosimeter.
- table S4. Values of the components used in the device for the four-color spectrometer.
- Legends for movies S1 to S3

Other Supplementary Material for this manuscript includes the following:
(available at advances.sciencemag.org/cgi/content/full/2/8/e1600418/DC1)

- movie S1 (.avi format). A movie of switching LEDs during the blood oximeter device operation.
- movie S2 (.avi format). A movie of switching LEDs during the four-color spectrometer device operation.
- movie S3 (.avi format). A movie of switching LEDs during the four-color spectrometer device operation in water.

Supplementary Materials

Here we report a detailed description of the process to fabricate and transfer the devices. Additional pictures and measurements are also reported to complement those included in the main text.

note S1. Fabrication procedure for devices

Sample preparation

1. Spin coat Cu foil (5 μm thick, Oak Mitsui Micro-thin series) with polyimide (PI2545; HD Microsystems, 3000 rpm for 30 s)
2. Anneal at 150 °C for 5 min
3. Anneal at 250 °C under vacuum for 75 min
4. Clean a glass slide (Acetone, IPA rinse)
5. Spin coat glass slide with polydimethylsiloxane (PDMS; Sylgard184, 3000 rpm for 30 s)
6. Laminate PI-coated Cu foil onto PDMS coated glass slide with PI side down

1st metal layer patterning (stretchable coil pattern)

7. Pattern photoresist (PR; AZ 4620, 3000 rpm for 30 s, anneal at 110 °C for 3 min) through iron oxide mask with UV irradiance for 300 mJ cm^{-2}.
8. Develop in aqueous developer (AZ400K, diluted 1:2 volume ratio, ~40 s)
9. Wet etch with Cu etchant (CE-100, Transense)
10. Remove PR with Acetone, IPA rinse

VIA hole patterning

11. Spin coat with PI (2000 rpm for 30 s)
12. Anneal at 150 °C for 5 min
13. Anneal at 250 °C under vacuum for 75 min
14. Pattern photoresist (PR; AZ 4620, 3000 rpm for 30 s, anneal at 110 °C for 3 min) through iron oxide mask with UV irradiance for 300 mJ cm^{-2}.
15. Develop in aqueous developer (AZ400K, diluted 1:2 volume ratio, ~40 s)
16. Etch PI (RIE; 200 mTorr, 20 sccm O_2, 150 W, 900 s)
17. Remove PR with Acetone, IPA rinse
18. Remove oxide with oxide remover (Flux, Worthington)

2nd layer patterning (interconnects)

19. E-beam 1 μm Cu

20 Pattern PR AZ4620

21 Wet etch Cu with Cu etchant

22 Remove PR with Acetone, IPA rinse

Device isolation

23 Spin coat with PI (2000 rpm for 30 s)

24 Anneal at 150 °C for 5 min

25 Anneal at 250 °C under vacuum for 75 min

26 E-beam 50 nm SiO_2

27 Pattern PR AZ4620

28 Etch SiO_2 (50 mTorr, 40 sccm CF_4, 100 W, 10 min)

29 Etch PI (300 mTorr, 20 sccm O_2, 200 W, 1800 s)

30 Clean with Acetone, IPA rinse

31 Remove oxide with oxide remover

Substrates preparation

32 **Pulse-rate monitor:** An ultrathin (~25 μm) medical adhesive (Acrylic adhesive, Scapa Healthcare)

33 **Blood oximeter:** An ultrathin low modulus silicone elastomer (Silbione) coated black textile substrate

34 **UV dosimeter:** ~300 μm of silicone elastomer (PDMS)

35 **Four-color spectrometer:** ~500 μm of silicone elastomer (Ecoflex)

Transfer

36 Pick up the pattern with water soluble tape

37 E-beam Ti (5 nm) / SiO_2 (100 nm) on water soluble tape

38 Activate each substrate (Silicon elastomer) with UV-Ozone exposure for 3 min

39 Bond water soluble tape to PDMS with patterns facing down

40 Remove water soluble tape with water

Chip assembly

41 Remove oxide with oxide remover

42 Solder with indium/silver soldering paste (~165 °C)

43 Encapsulate with silicon elastomers

note S2. FEA and optimization of device layout

The commercial software ABAQUS (ABAQUS Analysis User's Manual 2010, V6.10) was used to study mechanics of the devices and to aid in the design of optimized layouts. The compliant substrates (PDMS and Ecoflex) were modeled by hexahedron elements (C3D8R) while the stiff films (Cu and PI) were modeled by composite shell elements (S4R). Three mesh densities were used to ensure the accuracy and convergence of numerical results, with the numbers of elements to be 80000, 320000 and 1200000 for the coarse, medium, and fine meshes, respectively. For the medium mesh, the minimal mesh size was ~0.1 of the smallest feature dimension (e.g., minimum fillet radius). All meshes showed the same distributions of displacement and strain while the difference in the maximum strain between medium and fine meshes was ~1.2 %.

The positions of the chips and the widths of serpentine interconnects were optimized to satisfy some competing requirements from mechanics and electrical designs. For example, narrow interconnects improve the elasticity stretchability, but increase the electrical resistance. An iterative optimization process was adopted to carefully balance these and other mechanical and electric considerations. The position of the chip was optimized to avoid entanglement of interconnects and contact between components.
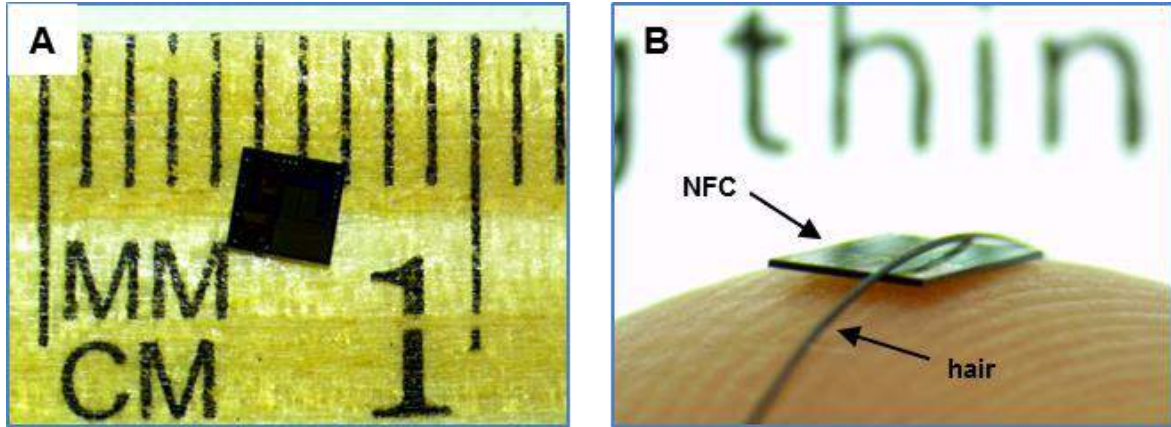
fig. S1. Size and thickness of the AMS SL13A NFC chip. (A) The size of the bare die is 2.38 mm x 2.38 mm. **(B)** The thickness of the die is ~100 μm, which is comparable to a human hair.
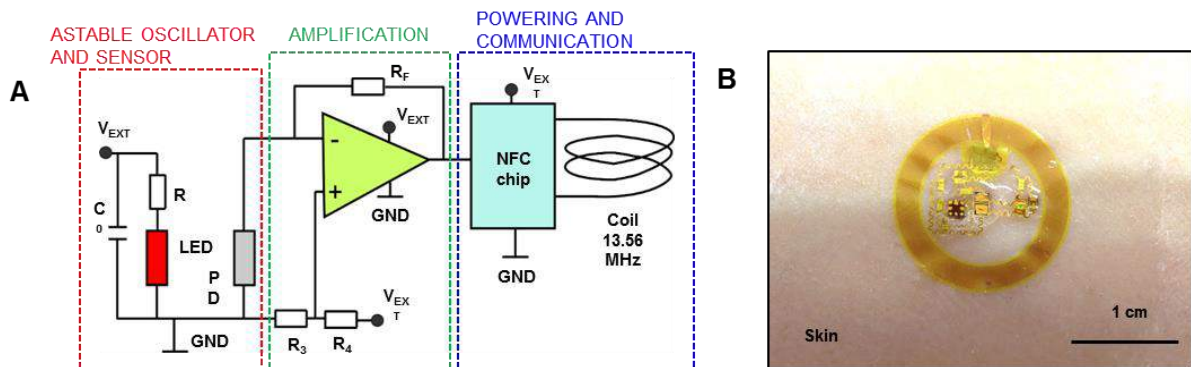
fig. S2. Circuit diagram of the pulse rate monitoring device and an image of the device mounted on the forearm. (A) The device consists of one led and one photodetector which is reverse biased and one amplifier in trans-impedance configuration. The output signal of the amplifier is connected to the analog input of the analog/digital converter of the NFC chip and transmitted wirelessly to an NFC reader. **(B)** A picture of the device mounted on the forearm for pulse monitoring.

table S1. Values of the components used in the device for heart rate monitoring. The names of the components refer to the circuit schematic of fig. S2A.

Component	Value
R_f	100 kΩ
R	681 Ω
C_0	1 μF
R_3	2.37 kΩ
R_4	23.7 kΩ
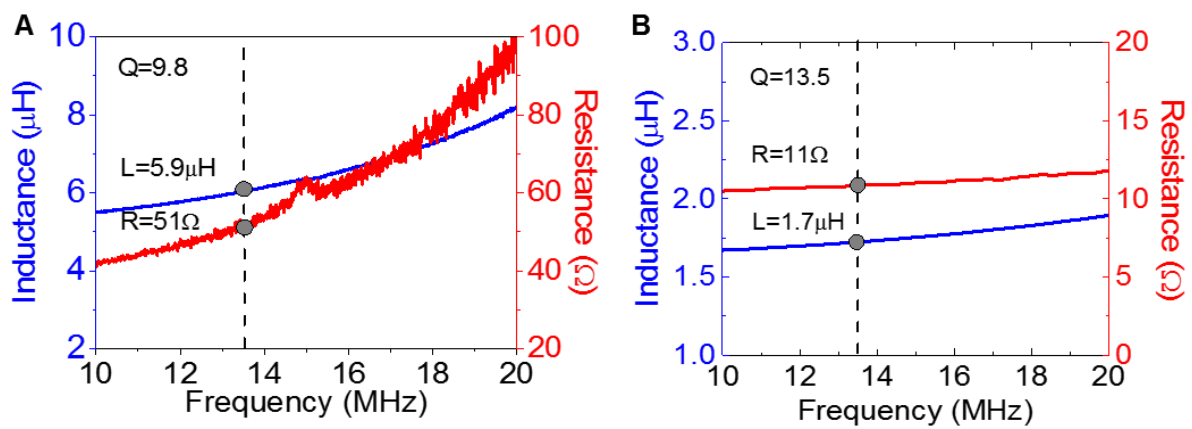
figure S3: Coil characterization. (A) Inductance and resistance of a circular coil at 13.56 MHz. **(B)** Inductance and resistance of a rectangular coil at 13.56 MHz.
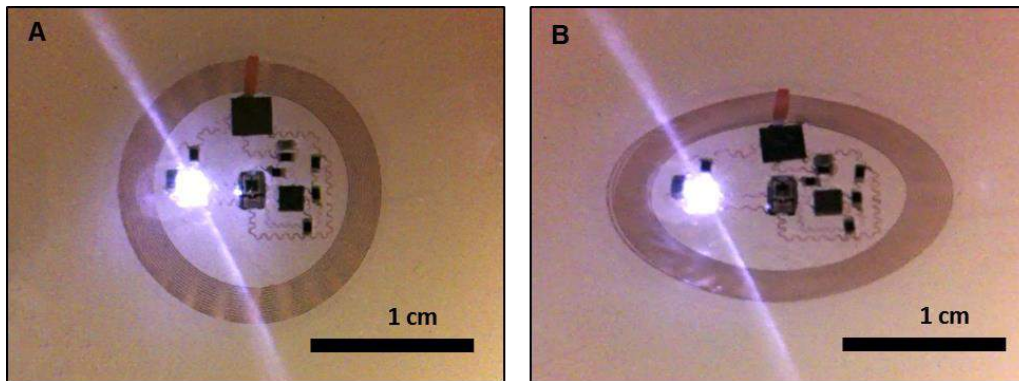
fig. S4. Device functionality. Pictures of the pulse rate monitoring device **(A)** before and **(B)** after 30 % stretching.
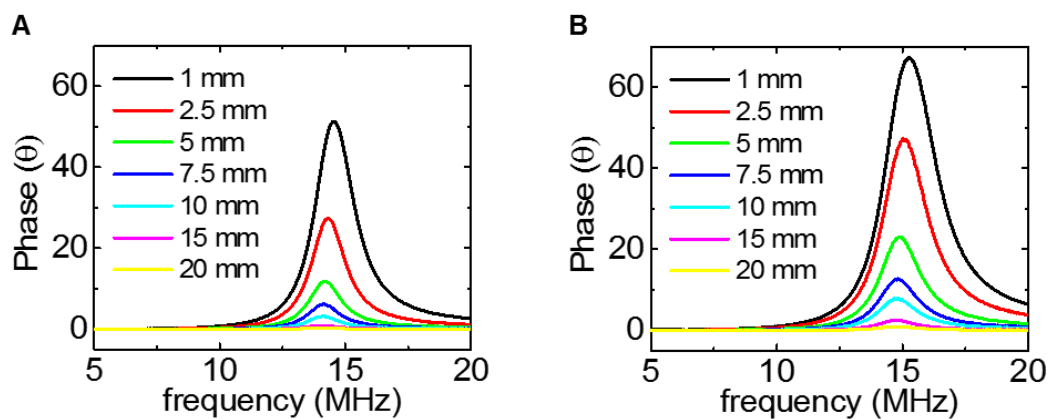
fig. S5. Inductive coupling for various operating distances between the primary and secondary coil. (A) Phase responses of a circular coil at 13.56 MHz for distance ranging from 1 mm to 20 mm in the case of parallel alignment. **(B)** Phase responses of a rectangular coil at 13.56 MHz for distance ranging from 1mm to 20 mm in the case of parallel alignment.
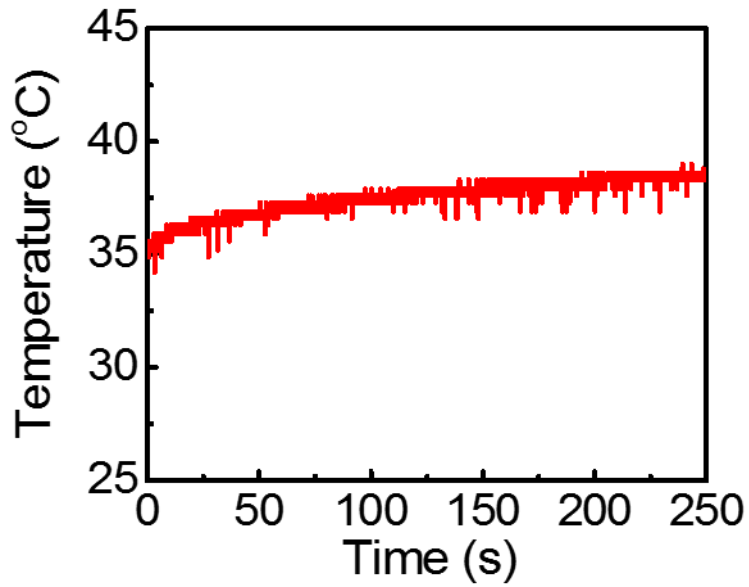
fig. S6. Temperature change during operation.

table S2. Values of the components used in the oximeter. The names of the components refer to the circuit schematic of Fig. 3B. The values for the R_1C_1 and R_2C_2 tanks are set in such a way that the switching frequency of the LEDs is 2-3 times smaller than the maximum sampling rate of the ADC (25Hz).

Component	Value
R_f	511 kΩ
R	681 Ω
R_1	19.6 kΩ
R_2	28.7 kΩ
C_0	10 μF
C_1	4.7 μF
C_2	4.7 μF
R_3	2.37 kΩ
R_4	23.7 kΩ
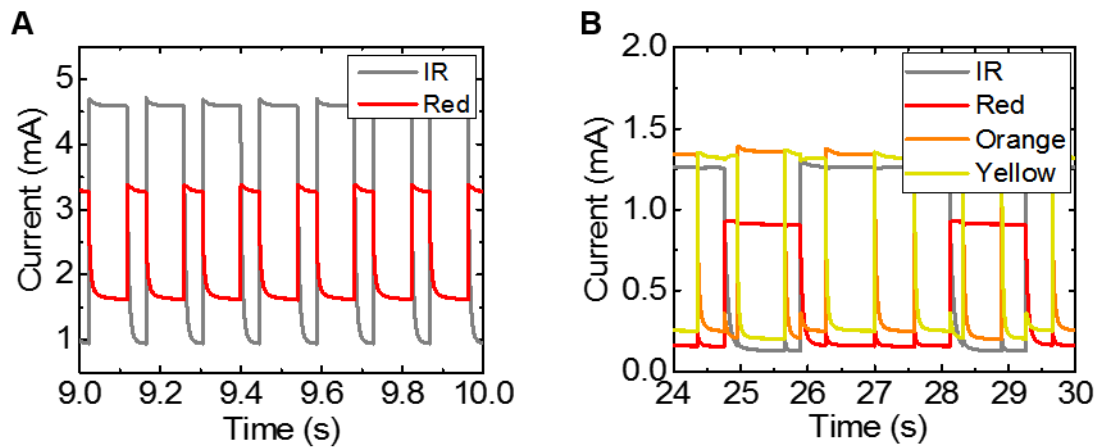
fig. S7. Current measurement of each LED during switching for (A) the oximeter and (B) the spectrometer.
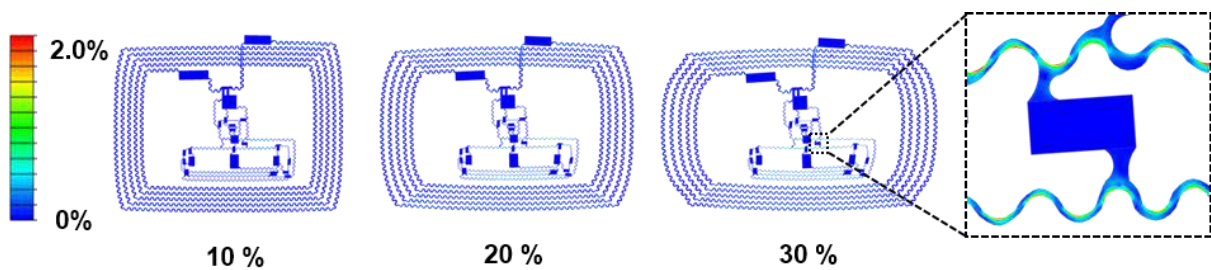
fig. S8. The distribution of maximum principal strain in the copper layer of the deformed oximeter device for the applied strain of 10 %, 20 %, and 30 %, respectively. The elastic stretchability of the device is ~8.5 % for 0.3 % yield strain of copper. For 30 % stretching, the maximum principal strain in copper is ~2.0 %, which is much lower than fracture strain (~5 %) of the copper.
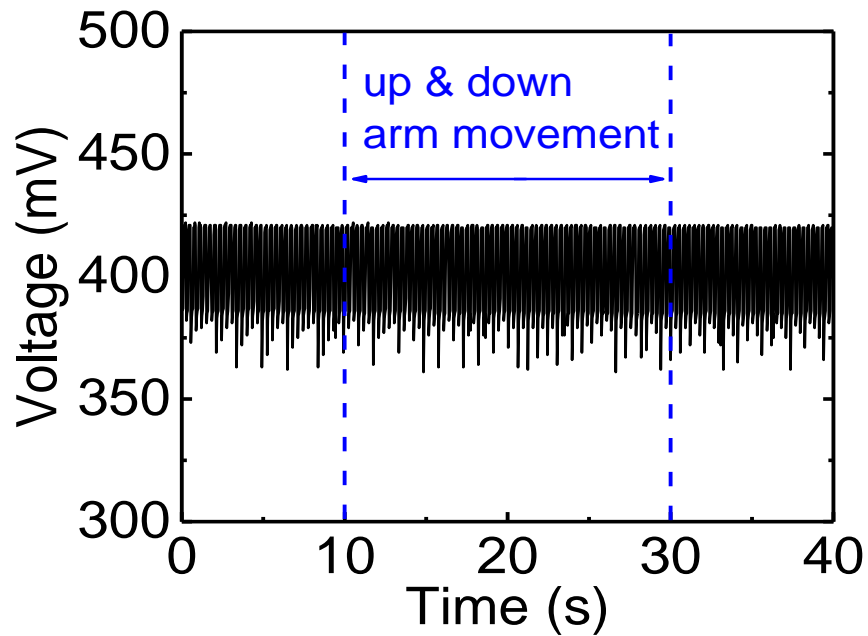
fig. S9. Data captured wirelessly from the forearm during up & down arm movement.
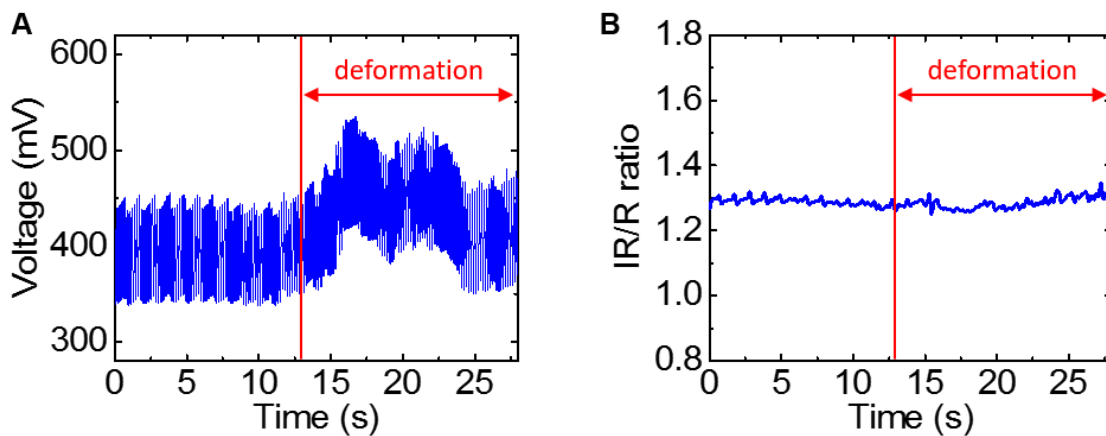
fig. S10. Data captured wirelessly from the forearm during deformation. (**A**) The raw data. (**B**) The ratio of IR component/Red component.
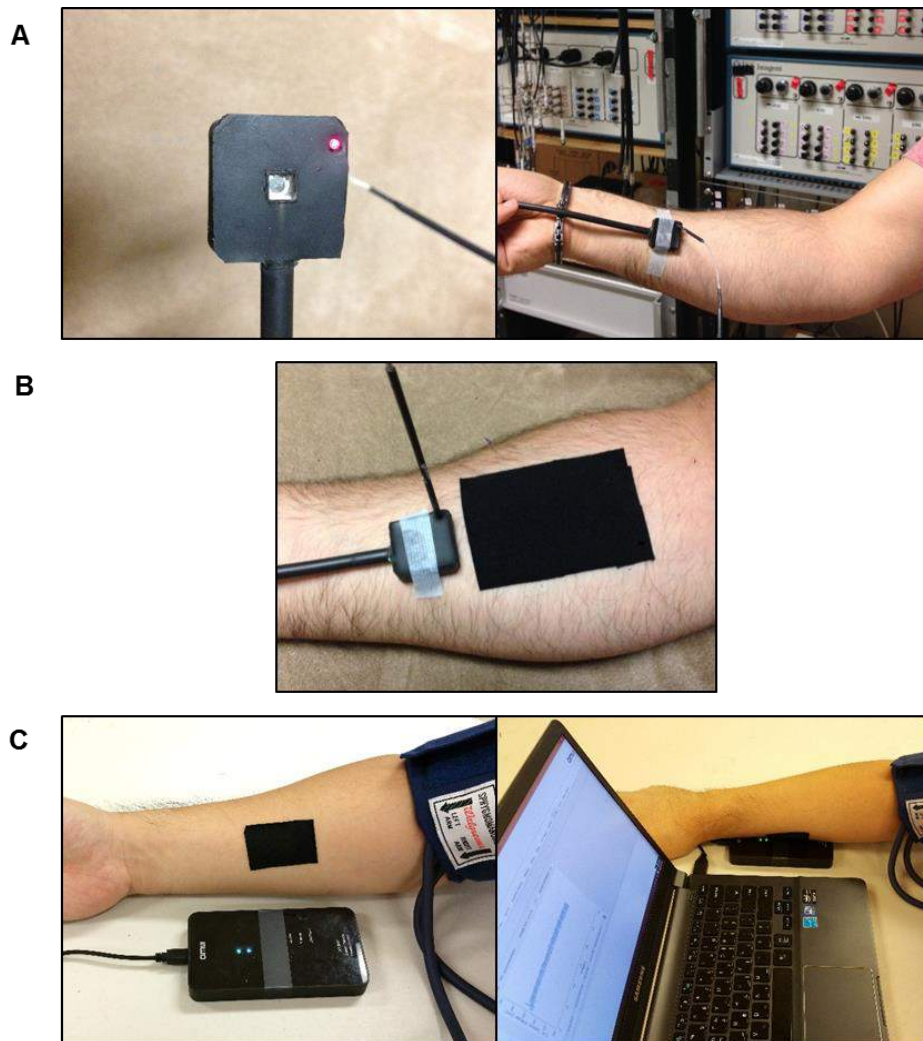
fig. S11. Wireless device benchmarked against a commercial NIRS system. **(A)** The commercial oximeter is equipped with laser diodes (830 nm and 690 nm wavelength) which transmit the light to the investigated surface using optical. Light is collected using a detector fiber bundle and measured by a photomultiplier. **(B)** Data are acquired synchronously from the two optical systems which are mounted on the forearm one close to the other. **(C)** During the experiment, an inflating cuff is placed around the participant's bicep, to occlude venous blood flow. During the recording, the subject undergoes 120 s of vein occlusion with 60 s of rest and recovery before and after the occlusion. The wireless sensor is read by an NFC reader provided from the chip manufacturer (AMS) which is connected to a PC.
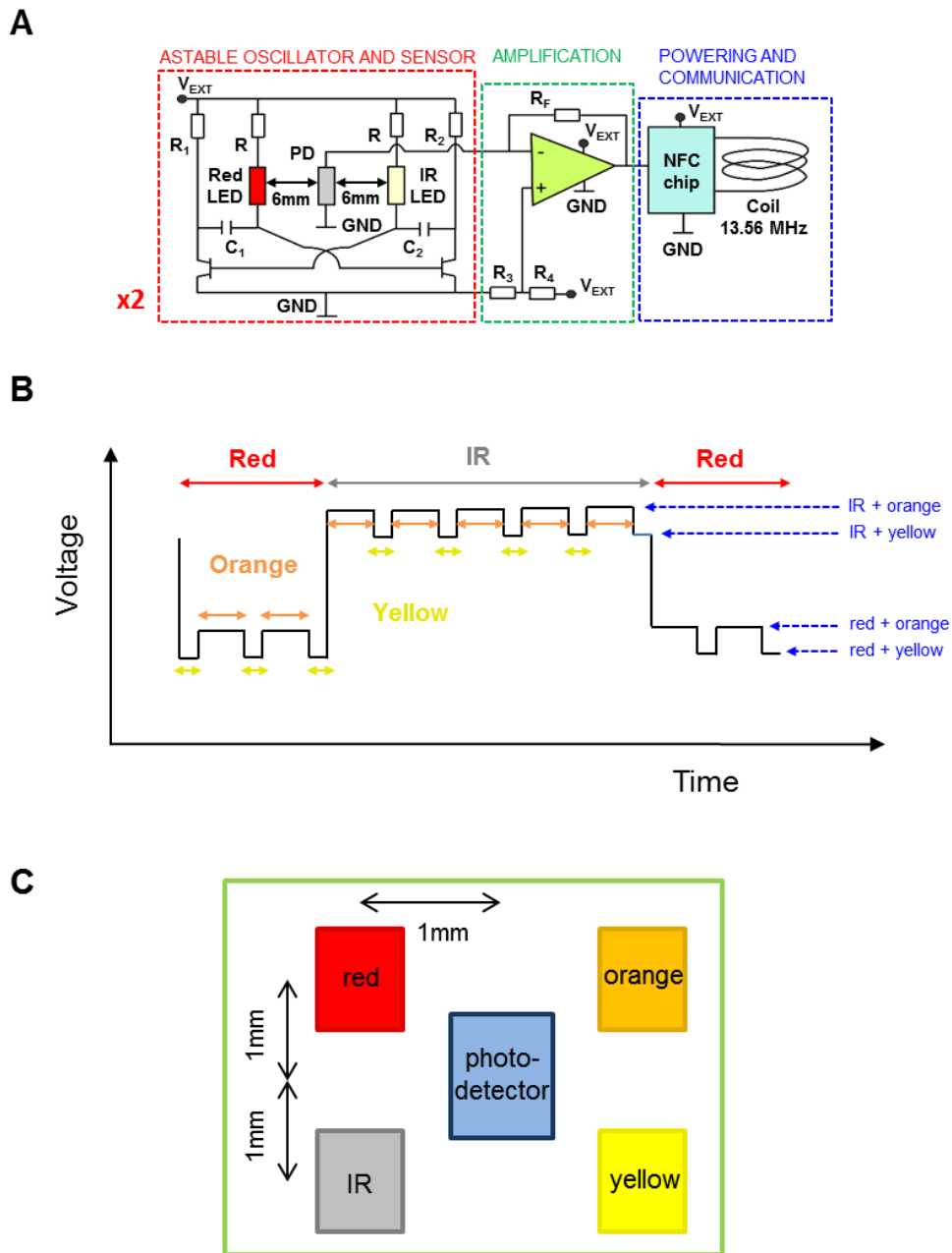
table S3. Values of the components used in the device for the UV dosimeter. The names of the components refer to the circuit schematic of Figure 3B. The distance between the LEDs and the photodiode is of 1 mm against the 6 mm of the oximeter and this leads to different values of resistors for the trans-impedance amplification and conditioning.

Component	Value
R_f	100 kΩ
R	681 Ω
R_1	51.1 kΩ
R_2	100 kΩ
C_0	10 μF
C_1	4.7 μF
C_2	4.7 μF
R_3	2.37 kΩ
R_4	23.7 kΩ
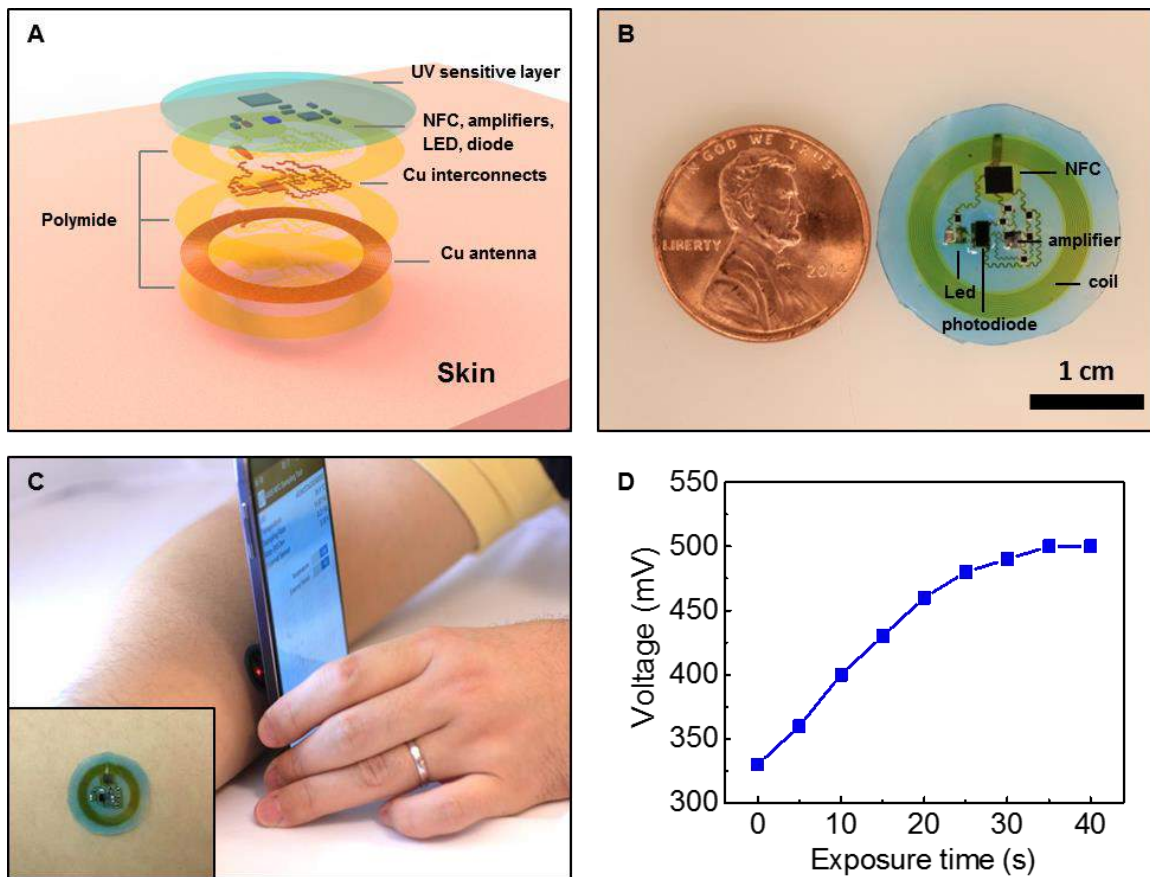
fig. S12. UV dosimeter with one-LED. **(A)** Exploded-view schematic illustration of a simplified version of the UV sensing device. **(B)** A picture of the device with a penny. **(C)** A picture of the device with a smartphone. (inset) A picture of the device mounted on a skin. **D)** The measurement of the UV sensor at varying UV exposure time.
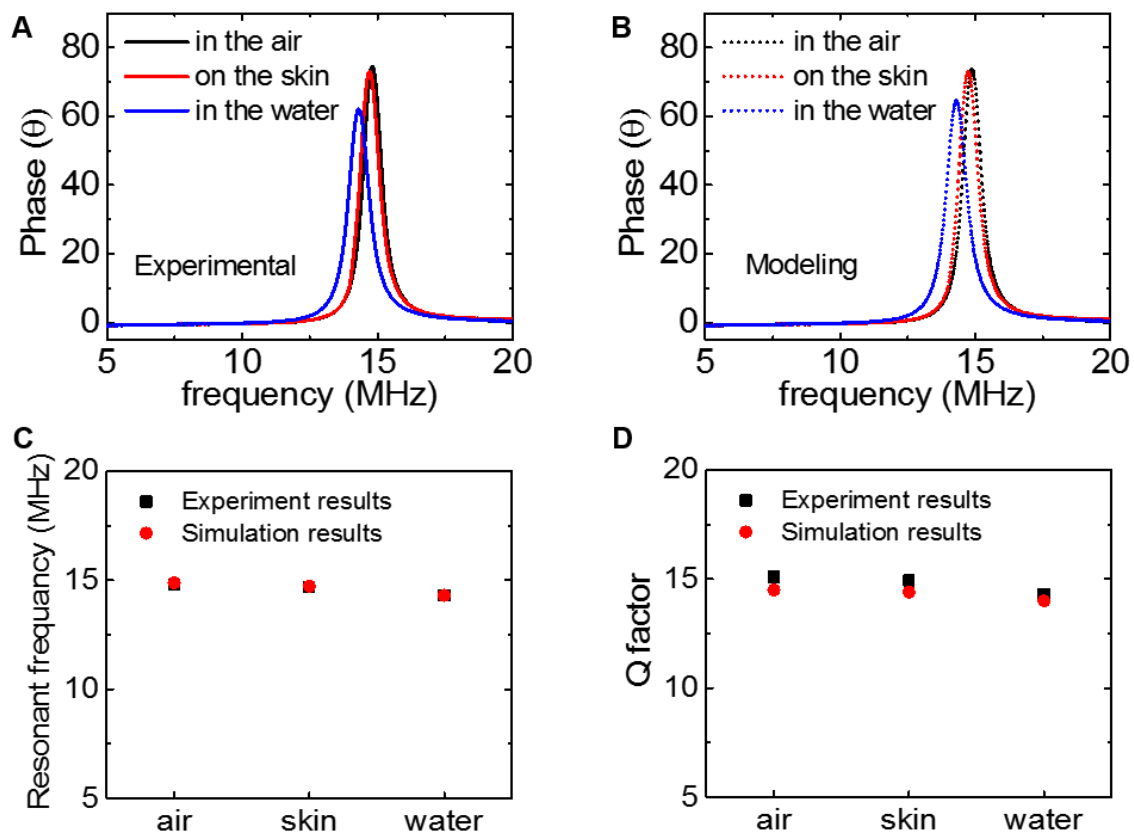
fig. S13. Four-color spectrometer. (A) A circuit diagram of the device, **(B)** illustration of measurement data obtained using a frequency multiplexing scheme and **(C)** geometry of the assembly of the LEDs and the photodetector.

table S4. values of the components used in the device for the four color spectrometer.
The names of the components refer to the circuit schematic of fig. S13A. R_{11}, R_{22}, C_{11}, C_{22} are the equivalent components to R_1, R_2, C_1, C_2, respectively, and refer to the components of the second astable oscillator circuit which is not shown for simplicity in the scheme of fig. S13A.

| Component	Value
R_f	100 kΩ
R	1 kΩ (for red/IR pair) 16.2 kΩ (for yellow/orange pair)
R_1	147 kΩ (red LED)
R_2	147 kΩ (IR LED)
R_{11}	100 kΩ (yellow LED)
R_{22}	100 kΩ (orange LED)
C_0	10 μF
C_1	20 μF
C_2	30 μF
C_{11}	10 μF
C_{22}	20 μF
R_3	14.7 kΩ
R_4	121 kΩ

fig. S14. **(A)** Measured phase responses of the device in the different mediums and **(B)** corresponding simulation results. **(C)** Measured and simulated changes in resonant frequency with different mediums. **(D)** Measured and simulated changes in Q factor with different mediums
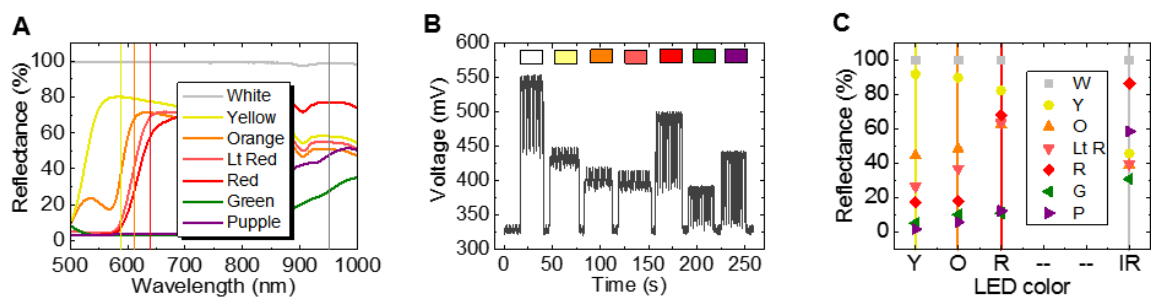
fig. S15. Colored PDMS measurement using the four color spectrometer. (A) The reflectance of seven different colored PDMS blocks. The vertical lines denote the wavelength of each LED light. **(B)** Wireless measurement of the seven different colored PDMS blocks. **C)** Calculated reflectance from measurement data of PDMS blocks with different colors. The graph appears agreeable with the reflectance graph (A).
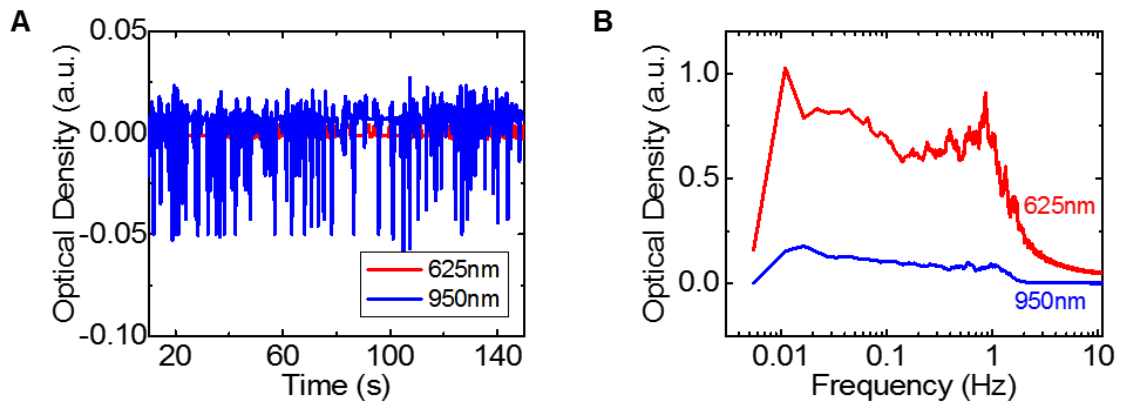
fig. S16. Noise optical density of the oximeter. The ultimate resolution of the devices was determined by performing a phantom measurement. The sensor was located on a side of a cubic phantom (100 mm x 100 mm x 100 mm) that resembled biological tissue optical properties.   Data were acquired for 180 seconds.   Noise estimation on the collected data was performed by computing the standard deviation of the electrical data variation over time. (**A**) Signal variability over the recorded period (estimated using standard deviation) was 1% at 950 nm wavelength and 2.49 % at 620 nm wavelength, respectively. (**B**) FFT of the optical density in (A).
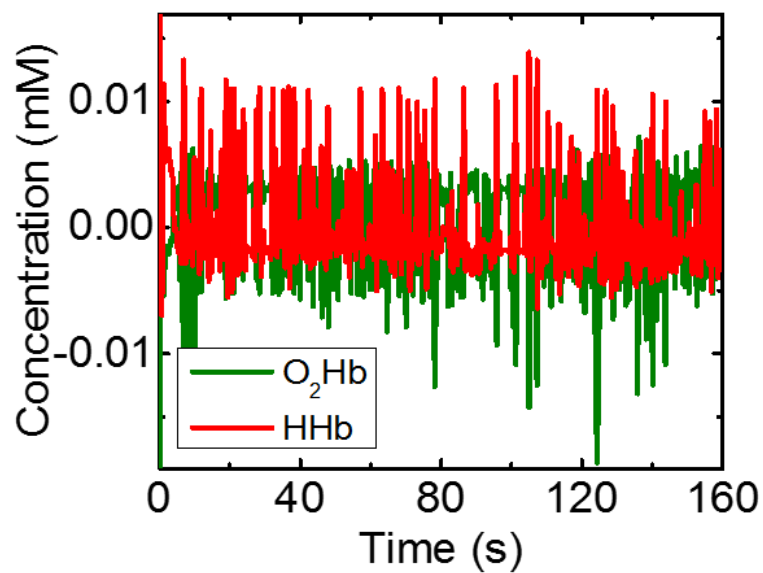
fig. S17. Ultimate concentration resolution of HHb and O₂Hb. The variability in the molar concentration of HHb and O₂Hb can be calculated starting from the optical density and using the Modified Lambert Beer Law. The estimated concentration variability is of ~0.050 mMol/L for both HHb and O₂Hb.
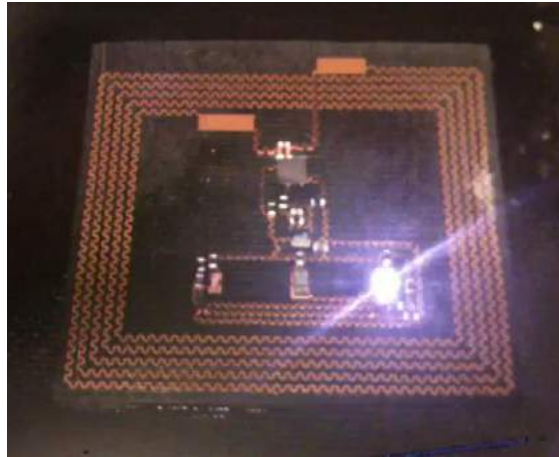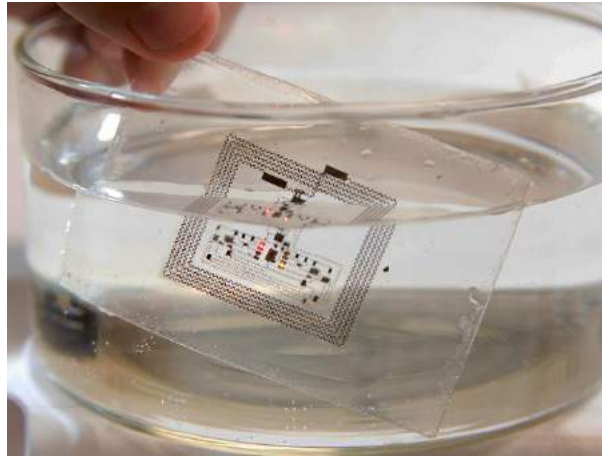
movie S1. A Movie of switching LEDs during the blood oximeter device operation.
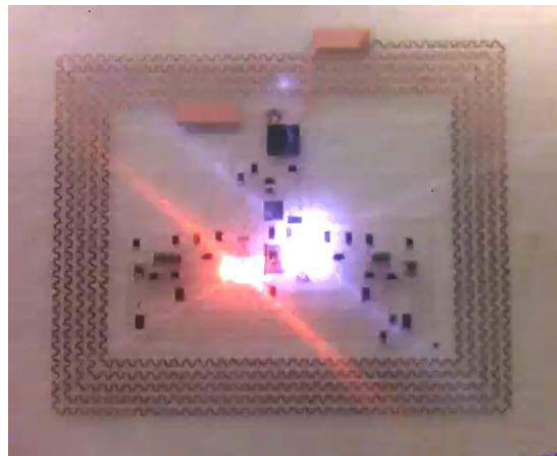
movie S2. A Movie of switching LEDs during the four color spectrometer device operation.

movie S3. A Movie of switching LEDs during the four color spectrometer device operates in water.